

REVIEW ARTICLE | JUNE 04 2024

Biomimic and bioinspired soft neuromorphic tactile sensory system

Kyowon Kang  ; Kiho Kim  ; Junhyeong Baek  ; Doohyun J. Lee  ; Ki Jun Yu 



Appl. Phys. Rev. 11, 021328 (2024)

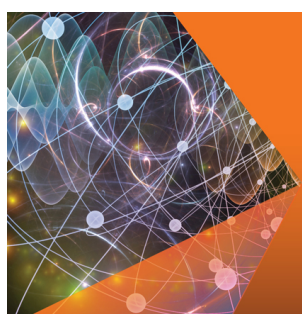
<https://doi.org/10.1063/5.0204104>



View
Online



Export
Citation



Journal of Applied Physics

Special Topic:

Disordered Materials at the Atomic Scale

Guest Editors: Jaeyun Moon, Matteo Baggio

Submit Today!

AIP Publishing

Biomimic and bioinspired soft neuromorphic tactile sensory system

Cite as: Appl. Phys. Rev. 11, 021328 (2024); doi: 10.1063/5.0204104

Submitted: 19 February 2024 · Accepted: 8 May 2024 ·

Published Online: 4 June 2024



Kyowon Kang,¹ Kiho Kim,¹ Junhyeong Baek,¹ Doohyun J. Lee,¹ and Ki Jun Yu^{1,2,a}

AFFILIATIONS

¹Department of Electrical and Electronic Engineering, Yonsei University, 50 Yonsei-ro, Seodaemun-gu, Seoul 03722, South Korea

²School of Electrical and Electronic Engineering, YU-Korea Institute of Science and Technology (KIST) Institute, Yonsei University, 50 Yonsei-ro, Seodaemun-gu, Seoul 03722, South Korea

^aAuthor to whom correspondence should be addressed: kijunyu@yonsei.ac.kr

ABSTRACT

The progress in flexible and neuromorphic electronics technologies has facilitated the development of artificial perception systems. By closely emulating biological functions, these systems are at the forefront of revolutionizing intelligent robotics and refining the dynamics of human-machine interactions. Among these, tactile sensory neuromorphic technologies stand out for their ability to replicate the intricate architecture and processing mechanisms of the brain. This replication not only facilitates remarkable computational efficiency but also equips devices with efficient real-time data-processing capability, which is a cornerstone in artificial intelligence evolution and human-machine interface enhancement. Herein, we highlight recent advancements in neuromorphic systems designed to mimic the functionalities of the human tactile sensory system, a critical component of somatosensory functions. After discussing the tactile sensors which biomimic the mechanoreceptors, insights are provided to integrate artificial synapses and neural networks for advanced information recognition emphasizing the efficiency and sophistication of integrated system. It showcases the evolution of tactile recognition biomimicry, extending beyond replicating the physical properties of human skin to biomimicking tactile sensations and efferent/afferent nerve functions. These developments demonstrate significant potential for creating sensitive, adaptive, plastic, and memory-capable devices for human-centric applications. Moreover, this review addresses the impact of skin-related diseases on tactile perception and the research toward developing artificial skin to mimic sensory and motor functions, aiming to restore tactile reception for perceptual challenged individuals. It concludes with an overview of state-of-the-art biomimetic artificial tactile systems based on the manufacturing–structure–property–performance relationships, from devices mimicking mechanoreceptor functions to integrated systems, underscoring the promising future of artificial tactile sensing and neuromorphic device innovation.

© 2024 Author(s). All article content, except where otherwise noted, is licensed under a Creative Commons Attribution-NonCommercial 4.0 International (CC BY-NC) license (<https://creativecommons.org/licenses/by-nc/4.0/>). <https://doi.org/10.1063/5.0204104>

TABLE OF CONTENTS

I. INTRODUCTION.....	1
II. RECENTLY DEVELOPED HIGH-PERFORMANCE PRESSURE SENSORS.....	2
III. BIOINSPIRED SOFT NEUROMORPHIC TACTILE SENSORY SYSTEM	6
A. Human skin-mimicking pressure sensors.....	6
B. Artificial synaptic devices.....	10
C. Artificial neuromorphic systems for the recognition of tactile information.....	12
D. Integrated neuromorphic tactile sensory systems for biomimicry of afferent and efferent neuron functions.....	14
IV. CONCLUSION AND FUTURE PERSPECTIVES.....	18

I. INTRODUCTION

The human nervous system, which comprises 100×10^9 neurons,^{1–6} intricately processes diverse external stimuli and transmits corresponding responses to various organs, operating a complex computation process that is achieved systemically with a limited number of neurons relative to the introduced information. Therefore, recent research has been dedicated to delving deeper into the intricacies of the human nervous system and advancing neuromorphic systems that closely biomimic its functionalities.^{7–22} Tactile sensation, as a primary sense in somatosensory functions, plays a crucial role in not only perceiving external pressures but also detecting potential threats from the surroundings, serving as a vital mechanism for human protection. The human tactile sensory system transforms many types of pressure (sharpness, vibration, roughness, etc.), perceived by tactile sensory cells

called mechanoreceptors, into electrical signals in the form of action potentials.^{19–21} These signals are transmitted through nerve fibers connected by synapses to the brain, where perceived information is decoded, allowing the recognition of the originations, types, and intensities of the applied pressures. The somatosensory cortex and motor cortex recognize the pressure information and subsequently transmit appropriate responses to organs.

Tactile sensors, which can be utilized in numerous applications ranging from biomimetic artificial skins to advanced touch and display panels, prosthetics, functional robotics, human–machine interfaces, e-skins, and electronic medical devices, are considered to be of utmost significance across various cutting-edge technologies. Tactile sensor can be categorized into various types according to their transduction methods, such as capacitive, piezoresistive, and triboelectric. In conjunction with the exploration of different transduction methods, diverse research has been conducted to explore various structures (pyramidal, micropillar, microdome, wrinkled, and porous structure) and materials (metallic or semiconductive materials, conductive polymers, carbon materials, ionic gels, etc.) for tactile sensing components.^{23–28} The skin senses the presence and magnitude of externally applied mechanical force, which is complex information, through four types of mechanoreceptors (Merkel cell, Meissner corpuscle, Pacinian corpuscle, and Ruffini ending) with different sensing mechanisms. Merkel cells are also known as Merkel–Ranvier cells or tactile epithelial cells, which are essential for light touch sensation. Merkel cells are abundant in highly sensitive skin like that of the fingertips and make synaptic contacts with somatosensory afferent nerve fibers which express PIEZO2, a mechanosensitive ion channel that responds to mechanical forces.²⁹ Spindle-shaped Ruffini corpuscle is sensitive to skin stretch and contributes to the kinesthetic sense of and control of finger position and movement.³⁰ Ruffini corpuscle registers mechanical deformation within joints, more specifically angle change as well as continuous pressure states, responding to it and showing very little adaptation.³¹ Meissner corpuscles consist of a cutaneous nerve ending responsible for transmitting the sensation of fine, discriminative touch and vibration.³² They can respond to skin indentations of $10\text{ }\mu\text{m}$ below and are most sensitive to low-frequency vibrations between 10 and 50 Hz. Additionally, Meissner corpuscles have been hypothesized to function in the relay of pain sensations, as some axons may express substance P and other nociceptive peptides.³³ The corpuscles respond to any stimuli within receptive field size of 3–5 mm in diameter with approximate uniformity, resulting in relatively limited spatial resolution. Pacinian corpuscles, also known as Vater-Pacini or lamellar corpuscles, are sensory receptors for vibration and deep pressure which are essential for proprioception.³⁴ Pacinian corpuscles have been found to be located adjacent to and within capsuloligamentous structures where they can provide reflexogenic feedback and offer indirect support regarding joint stability. These corpuscles are especially sensitive to vibrations, which they can sense the vibration even few centimeters away. Their optimal sensitivity is 250 Hz, and this is the frequency range generated upon fingertips by textures made of features smaller than $1\text{ }\mu\text{m}$.³⁵ Pacinian corpuscles respond when the skin is rapidly indented but not when the pressure is steady, due to the layers of connective tissue that cover the nerve ending. Pacinian corpuscles have a large receptive field on the skin's surface with an especially sensitive center. Recently, tactile sensory neuromorphic devices have been introduced, which biomimic the mechanoreceptors of the human tactile

sensory system by integrating different sensing mechanisms of conventional tactile sensors into a single tactile sensor; complex externally applied pressure information is converted into electrical signals and can be precisely recognized.^{36,37}

In human tactile sensation, tactile information is rapidly conveyed to the somatosensory cortex through long neural fibers by action potentials, with the frequency of spikes in action potentials storing tactile information.^{38–40} The spike-shaped action potentials are transmitted to the next neuron through synapses. The tactile information in the form of action potentials is diffused electrochemically to multiple subsequent neurons simultaneously for efficient tactile information transmission, rather than conveying information in sequence from one neuron to the next. The chemical receptors at the front of the synapse recognize the diffused chemicals (neurotransmitter), undergo a decoding process, and transmit the information back in the form of action potentials.^{41–46} The tactile information action potentials are decoded and recognized in the cerebral cortex. Tactile sensation biomimicry has evolved beyond simply mimicking the physical properties of human skin by employing soft and flexible materials,^{47–49} which extends to biomimicking the underlying principles of the human tactile perception system, including sensing tactile stimuli, conveying potential signals, and processing and recognizing the tactile information with a single integrated system. Advanced biomimic soft tactile systems are integrated with artificial synapses [resistive random-access memory (RRAM), synaptic transistor]^{15,16,50–55} and artificial neural networks such as spike neural networks (SNNs)^{17,18,39,56} for information recognition. The ability to implement sensitiveness, adaptiveness, plasticity, and memory at the electronic system level demonstrates the promising potential for the development of advanced human-centric devices.

Single-system-integrated artificial tactile sensory systems are highlighted not only in the development of artificial neurons by the mimicry of human tactile perception but also in the implementation of human somatosensory feedback functions ultimately. Tactile sensing, which is essential for human interaction with the external environment, poses a significant issue, as skin-related diseases annually affect tens of thousands of patients, leading to difficulties in normal tactile perception. As a solution, research has been reported to develop artificial skin that mimics both the sensory and motor functions of human skin, aiming to reconstruct the tactile reception system for individuals facing challenges in tactile perception.^{19–22} This article showcases the evolution of state-of-the-art bioinspired artificial tactile sensory systems, extending beyond replicating the physical properties of human skin to integrating artificial synapses and neural networks for advanced information recognition (Fig. 1). In addition, the perspectives toward the future artificial tactile sensing and neuromorphic devices are provided.

II. RECENTLY DEVELOPED HIGH-PERFORMANCE PRESSURE SENSORS

In the endeavor to create sophisticated neuromorphic systems, a critical and fundamental requirement is the integration of exceptionally sensitive pressure sensors. These sensors must possess the capability to detect external pressures with unparalleled precision, highlighting the paramount importance of high sensitivity in enhancing the accuracy and functionality of the neuromorphic system.^{57–59} These sensors serve as a critical interface, enabling neuromorphic systems to interact with their environment in a manner similar to the

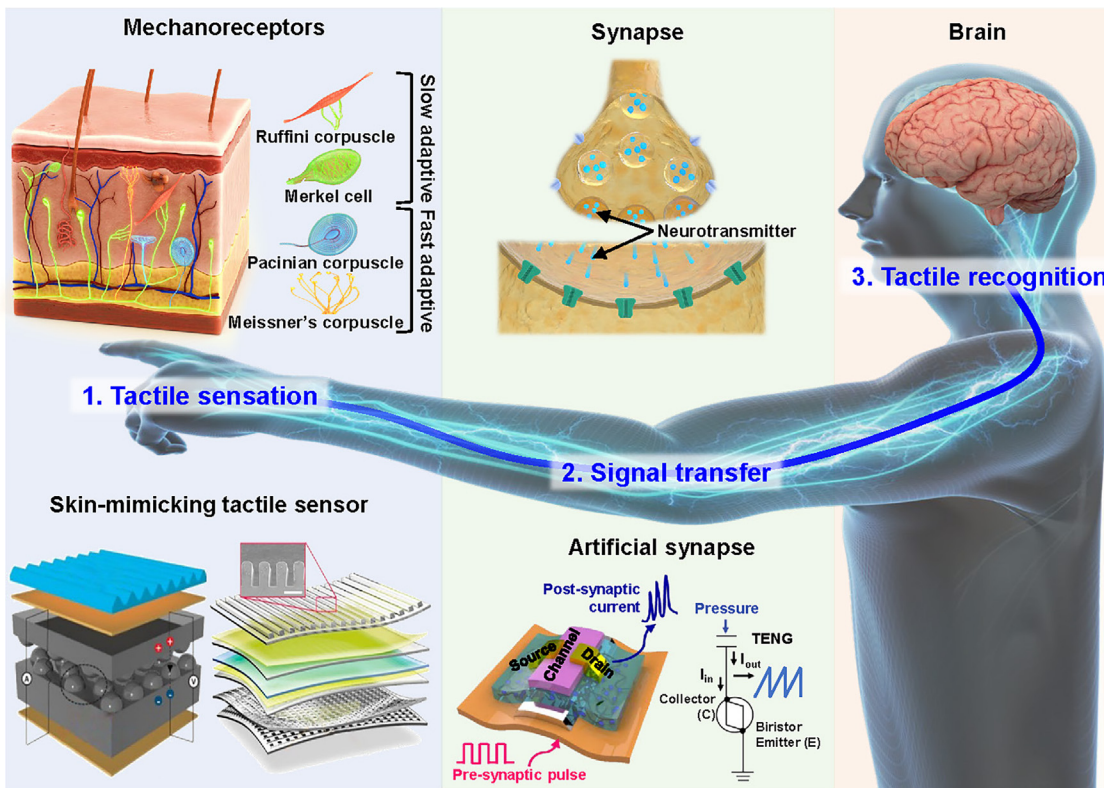


FIG. 1. Overall schematic of tactile recognition process and corresponding bioinspired tactile sensation related systems. Reprinted with permission from Park *et al.*, Sci. Adv. 1(9), e1500661 (2015). Copyright 2015 The Authors.³⁷ Reprinted with permission from Chun *et al.*, Nano Lett. 19(5), 3305–3312 (2019). Copyright 2019 American Chemical Society.⁸⁸ Reprinted with permission from Lee *et al.*, Nat. Commun. 11(1), 2753 (2020). Copyright 2020 The Authors.¹⁶ Reprinted with permission from Han *et al.*, Adv. Sci. 9(9), 2105076 (2022). Copyright 2022 The Authors.¹⁷

08 July 2024 19:26:15

response of the human nervous system to tactile stimuli. The sensitivity and accuracy of these sensors are paramount in ensuring the efficacy and responsiveness of the entire system. The mechanisms of pressure sensing can be categorized into four primary methods: piezo-capacitive,^{23,60–62} piezoresistive,^{25,63,64} triboelectric,^{26,65–67} and piezoelectric.^{27,68,69} The operation of each of these methods is based on different physical principles, offering unique advantages and challenges in the context of pressure detection.⁷⁰ Figure 2 and Table I show the structure, principles, and performance of recently developed pressure sensors using each of these methods.

Ongoing research on enhancing the sensitivity of pressure sensors across these four mechanisms is crucial for the advancement of neuromorphic systems. By improving the ability to detect external pressure accurately and sensitively, these sensors will play a crucial role in enabling neuromorphic systems to mimic human sensory and cognitive functions more effectively. Bai *et al.* demonstrated a piezocapacitive flexible pressure sensor that incorporates a graded intrafillable architecture (GIA) [Fig. 2(a)].²³ This design features microstructures of varying heights, known as protrusions, which are inherently unstable and can buckle or bend under compression. Additionally, this architecture incorporates complementary undercuts and grooves that accommodate the compressed protrusions, thereby providing extra compressibility and significantly increasing device sensitivity. Beyond

the surface undercuts, the introduction of a height variation in the distributed protrusions leads to a scenario where the electrode initially contacts shorter protrusions once the taller ones have collapsed. This process results in a progressively expanding area of contact between the GIA film and the electrode across a broad range of pressures. Simultaneously, the initial area of contact, A_0 , before pressure application is deliberately reduced. This reduction causes the relative change in contact area, $\Delta A/A_0$, of the GIA to markedly increase with rising pressure. This enhancement in the normalized contact area significantly boosts the specific capacitance, attributable to the electron double layer formation at the interface of the iontronic GIA film and electrode. As shown in Fig. 2(b), the iontronic GIA film contains a multitude of low-molar-concentration ion pairs, both positive and negative. Upon application of a voltage, the electrons on the electrode and the counter ions in the GIA converge within the contact area, just nanometers apart, thus amplifying the capacitance. A GIA-based iontronic sensor demonstrates a high sensitivity across a broad spectrum of pressures [Fig. 2(c)]. The average sensitivity of the sensor is $S_1 \approx 3302.9 \text{ kPa}^{-1}$ (or 3.3 Pa^{-1}) for pressures under 10 kPa . In the pressure bracket of $10\text{--}100 \text{ kPa}$, the sensitivity is $S_2 \approx 671.7 \text{ kPa}^{-1}$. Above 100 kPa , the sensor maintains a nearly linear response, exhibiting a sensitivity of around $S_3 \approx 229.9 \text{ kPa}^{-1}$, effective up to 360 kPa . This indicates very high sensitivity and an ultrawide pressure work

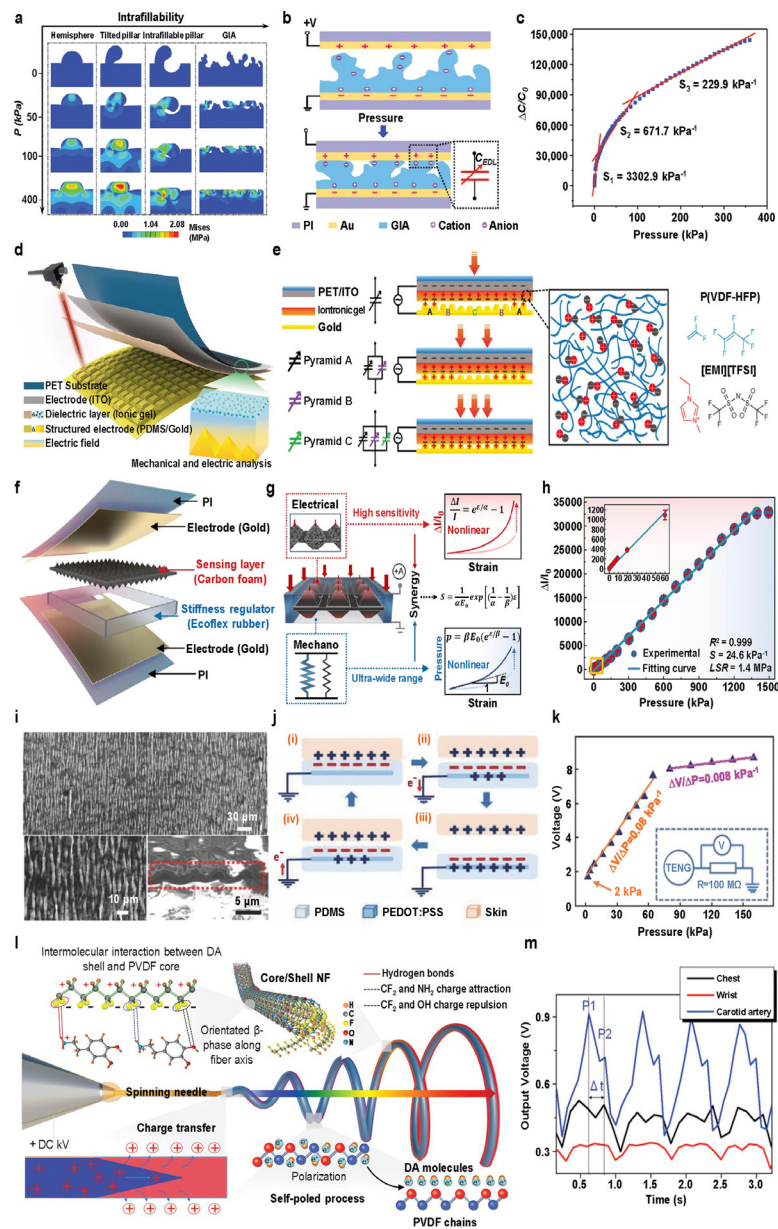


FIG. 2. Recently developed high-performance pressure sensors. (a) Stress distribution analysis from simulation outcomes across various structures subjected to pressures up to 400 kPa: a hemisphere; a tilted pillar, an intrafillable pillar without gradient, and the GIA. (b) Schematic illustration for the functioning of the iontronic pressure sensor before and after applying pressure. (c) Change of capacitance over the pressure range up to 360 kPa. Reprinted with permission from Bai et al., Nat. Commun. 11(1), 209 (2020). Copyright 2020 The Author(s).²³ (d) Schematic showing the design of the flexible iontronic pressure sensor. (e) Working mechanism of the iontronic pressure sensor. Reprinted with permission from Ruoxi et al., Nat. Commun. 14(1), 2907 (2023). Copyright 2023 The Author(s).²⁴ (f) Exploded view illustrating the design layout of the DPyCF@SR sensor. (g) Schematics showing the strategy to attain both high sensitivity and a broad linear range simultaneously. The synergy between the nonlinear elasticity of the SR and the nonlinear piezoresistivity of the DPyCF@SR results in the high linearity of the sensor. (h) Relative current change as a function of pressure ranging from 0 to 1400 kPa as measured from one DPyCF@SR sensor. S: sensitivity, LSR: linear sensing range (n = 3 samples; center, mean; error bars, s.d.). Reprinted with permission from Chen et al., Nat. Commun. 14(1), 6641 (2023). Copyright 2023 The Author(s).²⁵ (i) SEM image of a wrinkled PEDOT:PSS film on an elastic PDMS substrate. Left bottom inset shows the enlarged wrinkled morphology. Right bottom inset shows the cross-sectional view of the wrinkled film. (j) Schematic illustration of working mechanism for generating electricity. (k) Correlation between the maximum voltages measured across an external resistor (100 MΩ) and the applied contact pressure. The inset diagram displays the scheme of the WP-TENG based tactile sensor. Reprinted with permission from Wen et al., Adv. Funct. Mater. 28(37), 1803684 (2018). Copyright 2018 WILEY-VCH Verlag GmbH & Co. KGaA, Weinheim.²⁶ (l) Schematic of the arrangement and orientation of PVDF chains, influenced by intermolecular forces during the electropinning process used to create PVDF/DA core/shell NFs. (m) Piezoelectric voltage responses recorded by the PVDF/DA NFs sensor to blood pulsations at the neck, left wrist, and chest locations on a human volunteer. Reprinted with permission from Li et al., Adv. Mater. 33(3), 2006093 (2021). Copyright 2021 Wiley-VCH GmbH.²⁷

TABLE I. Performance comparison of recently developed high-performance pressure sensors.

Key materials	Tactile sensing mechanism	Recognizable types of applied pressure	Range of recognizable applied pressure	System components	Demonstrations	References
Polyvinyl alcohol (PVA)/H ₃ PO ₄ GIA	Capacitive	Vertically applied pressure	0–360 kPa	Pressure sensor	GIA-based micro-sensor arrays	23
Laser-ablated PMMA	Capacitive	Vertically applied pressure	0–2000 kPa	Pressure sensor	Fingertip pulse monitoring high precision weight scale, human robot interaction	24
Carbon foam, ecoflex rubber	Piezoresistive	Vertically applied pressure	0–1400 kPa	Pressure sensor	Physiological signal monitoring code-pressure double encryption	25
Wrinkled poly(3,4-ethylenedioxythiophene)-polystyrene sulfonate (PEDOT-PSS) electrode based triboelectric nanogenerator (TENG)	Tuboelectric	Vertically applied pressure	2–160 kPa	Pressure sensor	Active motion sensor for monitoring human body movement, 3 × 3 tactile sensor array	26
Poly(vinylidene fluoride) (PVDF)/dopamine (DA) nanofibers (NFs)	Piezoelectric	Vertically applied pressure	0–6 kPa	Pressure sensor	Implanted on the diaphragm in the abdomen and around the femoral artery to monitor diaphragm motion and arterial pulsation	27

range, making it exceptionally superior among existing piezocapacitive sensors. A compression and release test was conducted for over 5000 cycles at a peak pressure of 300 kPa, during which the sensor showed no signs of signal drift or fluctuations and exhibited minimal hysteresis throughout the testing cycles. The GIA-based iontronic pressure sensor is versatile, suitable for various applications such as health monitoring, electronic skins for tactile sensing, and pressure measurement in aerodynamics. Its intrafillable structure offers a universal design approach for other types of tactile sensors, enhancing sensitivity across a wide pressure spectrum. Yang *et al.* investigate employing a CO₂ laser with a Gaussian beam profile to create programmable structures like gradient pyramidal microstructures (GPM) for iontronic sensors.²⁴ This method decreases both the expense and the complexity of the process when compared to photolithography. The design of the flexible iontronic pressure sensor incorporates an iontronic dielectric layer placed between a structured bottom electrode and a top electrode made of polyethylene terephthalate (PET) combined with indium tin oxide (ITO) [Fig. 2(d)]. The functionality of this capacitive iontronic pressure sensor is influenced by the changing contact area between the ion layer and the structured pyramidal electrode under pressure. Its effective performance is attributed to an economically produced gradient pyramidal structure made from laser-ablated polymethyl methacrylate (PMMA), which is key to its operation. Figure 2(e) shows working mechanism of the iontronic pressure sensor. When an external voltage is introduced, electrons on the electrodes (both upper and lower) attract the ions of opposite polarity within the iontronic layer, causing them to accumulate at the electrode/ionic liquid (IL) interfaces, thus forming electric double layers (EDLs). At these interfaces, numerous electron-ion pairs are spaced only nanometers apart, acting like micro/nanoscale capacitors with very high capacitance. This

capacitance notably increases when the microstructured electrode is altered by pressure. Pyramidal structures of varying heights within the gradient microstructures are progressively deformed with increasing load pressure, expanding the sensor's range of detection. Furthermore, the gradient design reduces the initial contact area at the structured electrode/IL interface before pressure is applied, which enhances the normalized contact area and the capacitance change when pressure is exerted. This iontronic pressure sensor demonstrates a sensitivity of 33.7 kPa⁻¹ across a linear range up to 1700 kPa, with a detection threshold as low as 0.36 Pa and a pressure resolution of 0.00725% at a pressure level of 2000 kPa.

Figure 2(f) shows a piezoresistive pressure sensor with both high sensitivity and a wide linear range, which comprises a double-sided pyramidal carbon foam (DPyCF) array serving as the sensing layer and an elastomeric (Ecoflex rubber) spacer serving as the stiffness regulator (SR).²⁵ As shown in Fig. 2(g), Chen *et al.* utilized a DPyCF array for the sensing layer to achieve high sensitivity. This layer combines tapering microstructures and microscopic porosity, both of which are common methods for increasing the sensitivity of piezoresistive materials. The hierarchical three-dimensional porous structure of the layered carbon foam and its significant compressibility contribute to its pronounced nonlinear piezoresistivity. Furthermore, to broaden the scope of pressure detection, they incorporated an elastic spacer, SR, around the sensing layer. This SR is designed to distribute the load on the sensing layer evenly. High sensitivity at low pressures and effective pressure sensing at high pressures require the SR to exhibit stiffening behavior, or nonlinear elasticity, when compressed. This interplay of nonlinearities in both the elasticity of the SR and the piezoresistivity of the sensing layer leads to the enhanced linearity observed in the piezoresistive pressure sensor. The sensor exhibits a linear variation

($R_2 = 0.999$) of $\Delta I/I_0$ in an ultrawide range of 0–1.4 MPa with a high sensitivity of 24.6 kPa^{-1} , which outweighs the values of any piezoresistive pressure sensors found in the literature^{71–80} as depicted in Fig. 2(h). The output signal indicates that the sensor continues to function effectively without any significant performance degradation, even after 50 000 loading and unloading cycles. A design strategy that integrates the nonlinearities in mechanical and electrical behaviors to achieve high sensitivity and a broad linear range can be adapted and applied to other types of pressure sensors.

Wen *et al.* developed a stretchable and transparent wrinkled poly(3,4-ethylenedioxythiophene) polystyrene sulfonate (PEDOT:PSS) electrode-based triboelectric nanogenerator (WP-TENG), which was designed to serve as a biomechanical energy harvester, a human motion tracker, and an active touch sensor [Fig. 2(i)].²⁶ The electrical conductivity and the level of transparency of this wrinkled electrode are adjustable by the manipulation of the number of layers in the mask during the blade-coating procedure. By employing elastic polydimethylsiloxane (PDMS) as both the triboelectrification layer and a sealing material, they enabled the WP-TENG to operate effectively in a single-electrode configuration. Figure 2(j) illustrates the working mechanism of the WP-TENG. When the skin comes into contact with the WP-TENG, because of the contact electrification effect, electrostatic charges are transferred from the skin's surface to the PDMS surface until they reach a saturation point (state i). As the skin moves away from the PDMS, the electrostatic field created by the triboelectric charges induces electron flow through the external load, moving from the electrode to the reference electrode (ground). This movement leads to a buildup of free electrons in the electrode until equilibrium is reached (states ii and iii). When the skin moves toward the PDMS again, electrons flow back from the ground to the electrode, generating a reverse electric output signal (state iv). As the pressure increases from 2 to 60 kPa, the voltage increases linearly with a pressure sensitivity of 0.08 kPa^{-1} and a pressure detection limit of 2 kPa [Fig. 2(k)]. The energy harvesting and active sensing capabilities of WPTENG, which feature exceptional transparency and stretchability, show promising potential for development in applications including human-machine interactions, electronic skins, soft robotics, and wearable electronics.

In the field of piezoelectric pressure sensors, Li *et al.* reported a poly(vinylidene fluoride) (PVDF)/dopamine (DA) core/shell nanofiber (NF) fabricated by one-step electrospinning on a large scale, which showed significantly enhanced piezoelectric property with excellent stability.²⁷ The superior piezoelectric capabilities of this material can be linked to the abundant hydrogen bonds and dipole interactions, a result of the DA shell layer. This layer promotes the formation of β -phase domains and ensures that the dipoles are uniformly aligned. The seamless interface between DA and PVDF contributes to the stability of the β -phase in the NFs, making the PVDF/DA NFs a highly effective and flexible piezoelectric sensor [Fig. 2(l)]. The uniform distribution of $-\text{NH}_2$ groups along the molecular chains of DA and their likely robust interaction with the $-\text{CF}_2$ groups in PVDF led to the integration of DA into the PVDF electrospun solution as a diverse nucleating agent for β -phase crystallization. This inclusion enables the $-\text{NH}_2$ groups in DA to interact with the $-\text{CF}_2$ groups in PVDF, leading to the formation of strong and stable hydrogen bonds. Figure 2(m) presents the piezoelectric voltage signals obtained from the PVDF/DA NFs sensors at three distinct locations. Each voltage profile exhibited typical pulse-wave characteristics, namely, the systolic peak P1 and

dicrotic wave P2. These intricate details in the signals are critical, as they carry significant biomedical and physiological data, including indicators of arterial stiffness, coronary artery disease, and myocardial infarction. The durability of the core/shell PVDF/DA NFs was evaluated over more than 2000 continuous straining cycles under consistent operating conditions. The peak-to-peak voltage (V_{pp}) consistently maintained a steady level without any noticeable alterations. Additionally, after a 30-day immersion in phosphate buffer saline (PBS) solution, the core/shell PVDF/DA NFs preserved their superior piezoelectric functionality.

III. BIOINSPIRED SOFT NEUROMORPHIC TACTILE SENSOR SYSTEM

A. Human skin-mimicking pressure sensors

In human skin, the ability to highly perceive external mechanical signals originates from ionic mechanotransduction, a phenomenon integral to several physiological functions including the sense of touch, balance, and hearing.⁸¹ Primary mechanoreceptors are adept at sensing a wide array of tactile inputs from the environment. Notably, the Piezo2 protein, known as a mechanically activated ion channel, has been recently recognized as the key mechanical transducer in Merkel cells.^{29,82} Ionic mechanotransduction within these cells is facilitated by the movement of cations. This movement converts mechanical stimuli into temporary alterations in the ion balance of the cell plasma membrane, enabling the flow of ionic current through the membrane,⁸³ this ion movement is influenced by the poroelastic properties of structural proteins combined with interstitial fluid, aiding in long-distance transport.⁸⁴ Following this, the altered electrochemical signals are transmitted to the central nervous system (Table II).

Figure 3(a) depicts the mechanosensory system in mammalian skin, focusing on Merkel cell mechanoreceptors that manage ion movement, such as Na^+ , Ca^{2+} , and Cl^- , across the Merkel cell membrane along the papillary ridges at the epidermis–dermis boundary in the skin, linked to the nerve fibers of the central nervous system.³⁶ These ridges, rich in Merkel cells, boost tactile sensitivity. The Merkel cell complex features the Piezo2 nanochannel, a crucial transmembrane component. Normally closed to maintain a polarized membrane potential of -70 mV , the Piezo2 channel opens when mechanical pressure is applied, enlarging its cross-sectional area. This action forces cations from outside the cell into the cell, upsetting the ion equilibrium and causing cell depolarization. Jin *et al.* designed an artificial ionic mechanotransducer composed of a pillar-shaped ionic elastomer using ionic thermoplastic polyurethane (i-TPU) corresponding to Merkel cells within the periodic papillary ridge structure. When a voltage bias of 1 mV is applied, the interaction between the i-TPU and electrodes forms an electrical double layer, similar to the resting membrane potential of Merkel cells (-70 mV). However, the exertion of even a slight pressure on the ionic mechanotransducer results in the expulsion of ions that are almost free and not attached to TPU chains from the free space of the i-TPU matrix, disrupting the balance of ions. Figure 3(b) shows a significant increase in capacitance when pressure is applied, even though the contact area between the i-TPU and gold electrode remains unchanged. This phenomenon can be attributed to the increased formation of ion pairs within the electrical double layer when pressure is applied. Furthermore, under identical pressure and voltage conditions, the ionic mechanotransducer with a patterned i-TPU film shows a greater capacitance change compared to the flat

TABLE II. Performance comparison of recently developed bioinspired soft neuromorphic tactile sensory systems.

Key materials	Tactile sensing mechanism	Recognizable types of applied pressure	Range or recognizable applied pressure	System components	Demonstrations	References
Ionic thermoplastic polyurethane	Piezocapacitive	Vertically applied pressure	0.1–50 kPa	Pressure sensor	Sensing a wide range of pressures in human-adaptive tactile systems	36
PVDF, rGO	Piezoresistive, ferroelectric	Vertically applied pressure, slip	0–49.5 kPa	Pressure sensor, temperature sensor	Simultaneous monitoring of artery pulse pressure and temperature, texture perception	37
Graphene, TENG	Piezoresistive, triboelectric	Vertically applied pressure, slip	0.1–100 kPa	Pressure sensor, vibration sensor	Classifying 12 fabrics possessing complex patterns with 99.1% classification accuracy	88
Tactile sensor: PDMSMPU0.4-IU0.6, methyl isobutyl ketone (MIBK), PDMS RRAM: TiO ₂	Capacitive	Stretching and vertically applied pressure	0%–60% (stretching strain) 0–0.9 kPa (pressure)	Pressure sensor, artificial synapse, photonic actuator	Applied pressure pattern recognition and quantum-dot light-emitting diode (QLED) feedback of 5 × 5 array	15
Barium titanate nanoparticle (BT NP)/P[VDF-trifluoroethylene(trfe)] nanocomposite	Triboelectric-capacitive	Vertically applied pressure	0–3 kPa	Pressure sensor, ferroelectric organic field-effect transistor (Fe-OFET) based artificial synapse	Tactile sensing memory demonstration without any other storage device	16
Tactile sensor: Al, PTFE signal conversion: Si-based bipolar junction transistor (BJT)	Triboelectric	Vertically applied pressure	3.2–5 kPa	Pressure sensor, biristor neuron, SNN	Handwritten 10 digits recognition	17
Tactile sensor: PDMS, PEDOT:PSS	Resistive	Vertically applied pressure, slip, local curvature, object hardness	...	Pressure sensor, temperature sensor, decoder	Slip detection, local curvature and harness classification	18
Temperature sensor: Polycaprolactone (PCL):Ni	Resistive	Vertically applied pressure	0–80 kPa	Pressure sensor, organic ring oscillator, synaptic transistor	Cockroach efferent nerve stimulation	19
Tactile sensor: Carbon nanotube (CNT) Organic ring oscillator: HFO ₂ , C12-PA, Pentacene Synaptic transistors: polymer semiconductor (P1), Ion gel	Resistive	Vertically applied pressure	0–50 kPa	Pressure sensor, temperature sensor, organic ring oscillator, artificial synapse	Mouse sciatic nerve stimulation	20
Tactile sensor: CNT Organic ring oscillator: Nitrile butadiene rubber, Poly(styrene-ethylene-butylene-styrene) (SEBS), Octadecyltrimethoxysilane (OTS), conjugated-polymer/elastomer phase separation-induced elasticity (CONPHINE) Artificial synapse: Ionic conducting elastomer, single ion conductor, Poly[(1-vinyl-3-propyl-imidazolium) bis(trifluoromethanesulfonyl)imide] (PiTFSI), Imidazolium, azide cross-linker	Resistive	Vertically applied pressure	0–50 kPa	Pressure sensor, temperature sensor, organic ring oscillator, artificial synapse	Mouse sciatic nerve stimulation	20

TABLE II. (Continued.)

Key materials	Tactile sensing mechanism	Recognizable types of applied pressure	Range or recognizable applied pressure	System components	Demonstrations	References
Tactile sensor: micro-cracked Pt	Resistive	Vertically applied pressure	0–100 kPa	Pressure sensor, signal modulation circuit, neural interface electrodes	Rat sciatic nerve stimulation, layer-by-layer skin regeneration	21
Artificial skin: fibrin, collagen						
Neural interface electrodes: genipin, gelatin						
Tactile sensor: BaTiO ₃ , rGO, PDMS	Piezoresistive (slow-adaptive, SA), piezoelectric (fast-adaptive, FA)	Vertically applied pressure, surface texture	0–100 kPa	Pressure sensor, artificial mechanoreceptor neuron board, deep learning algorithm	Rat efferent nerve stimulation, fabric texture recognition	22

i-TPU film, which is particularly more pronounced at higher voltage biases. Also, high stability in capacitance change was achieved when responding to dynamic pressures (100 Pa, 1, 10, 20, and 30 kPa) using the patterned i-TPU under a 1 mV condition. This suggests that the introduction of the pillar structure in the i-TPU increases the interface contact area with the electrodes, thereby improving the sensing capability of the ionic mechanotransducer.

Park *et al.* presented electronic skins (e-skins) inspired by human skin, which mimicked the complex structures and functionalities of the sensory system of human fingertips.³⁷ These e-skins are crafted from flexible, microstructured ferroelectric films [Fig. 3(c)] and are designed to enhance the recognition and differentiation of various tactile stimuli, including both static and dynamic pressure, as well as temperature and vibration. To emulate the dynamic touch and temperature sensing capabilities of human skin, these e-skins utilize the piezoelectric and pyroelectric responses of ferroelectric polymer composites made from PVDF and reduced graphene oxide (rGO). They address the inherent limitation of these ferroelectric e-skins in detecting continuous static pressures by employing a piezoresistive shift in the contact resistance found in the interwoven microdome structures within the rGO/PVDF composites. An external force can lead to deformation, subsequently causing changes in the contact area among the interlocking microdomes. This, in effect, results in alterations in contact resistance that depends on the pressure applied. Over 5000 repetitive cycles at a frequency of 0.3 Hz and a normal force of 20 kPa, the e-skins displayed no significant deterioration. To demonstrate the ability of the e-skin to discern temperature and pressure changes, they tested it with water-filled glass vials at varied temperatures and pressures [Fig. 3(d)]. Initial tests at 0.54 kPa and 23 °C showed constant resistance, indicating no thermal impact on the e-skin. However, during both loading and unloading, notable resistance change was observed because of the thermal gradient and equilibrium. This change became more pronounced with higher temperatures, showcasing the temperature sensitivity of the e-skin. When combining pressure with temperature changes, these variations could be detected by the differences in the stabilized resistance values, distinct from the immediate changes caused by temperature alone. These results confirm that the interlocked ferroelectric e-skins are capable of

concurrently identifying and distinguishing temperature and pressure changes, thanks to their piezoresistive and pyroelectric characteristics.

Mechanoreceptors are sensory neuron endings that react to mechanical stimuli by altering membrane potential, typically located at the periphery of A β -axon terminals.^{85,86} These receptors are divided into two categories: slow-adaptive (SA) and fast-adaptive (FA) mechanoreceptors.²² SA mechanoreceptors, like Merkel cells and Ruffini corpuscles, exhibit slow-adapting responses (SA type I and SA type II) and are sensitive to continuous static pressure. Conversely, FA mechanoreceptors, including Meissner and Pacinian corpuscles, are adept at sensing vibrations or high-frequency dynamic pressures, particularly at the end of fast-adapting afferents (FA type I and FA type II).⁸⁷ Tactile information gathered by these receptors is conveyed to the cerebral cortex for further processing, including memory and learning, through synaptic. Chun *et al.* developed an artificial neural tactile sensor (NTS) by combining an SA mechanoreceptor-like interlocking graphene sensor and an FA mechanoreceptor-like TENG sensor, both featuring fingerprint-like micropatterns [Fig. 3(e)].⁸⁸ The lower graphene film sensor array, which comprises 400 pixels, is capable of sensitive static pressure measurement within the range typical for human touch (1.63 kPa^{-1} for 0–6 kPa), as well as capturing pressure distribution with 100 pixels/cm². The sensor demonstrated highly consistent piezoresistive responses throughout 10 000 repetitive loading-unloading cycles, with vertical pressures of 10 and 100 kPa applied. The upper TENG sensor, with its single-sensor design, effectively detects dynamic pressures or vibrations. The graphene-based sensor, which mimics SA mechanoreceptors, and the TENG device, mimicking FA mechanoreceptors, produce output signals that closely resemble the firing patterns of human skin SA and FA mechanoreceptors, respectively. For the SA mimicking sensor, the variation in sensitivity due to applied pressures is linked to the distinct operational modes of the graphene suspension of nanoplatelets (GNP) film sensor with an interlocking percolative structure. At lower pressure levels, the interlocking action between the upper and lower GNP sheet films initiates a stage of mechanical and electrical connectivity, causing a swift reduction in resistance. When the electrical connection becomes steady at a pressure near 6 kPa, merging the upper and lower films into a unified GNP layer, there is a gradual rise in the pressure sensitivity, which is a result of enhanced

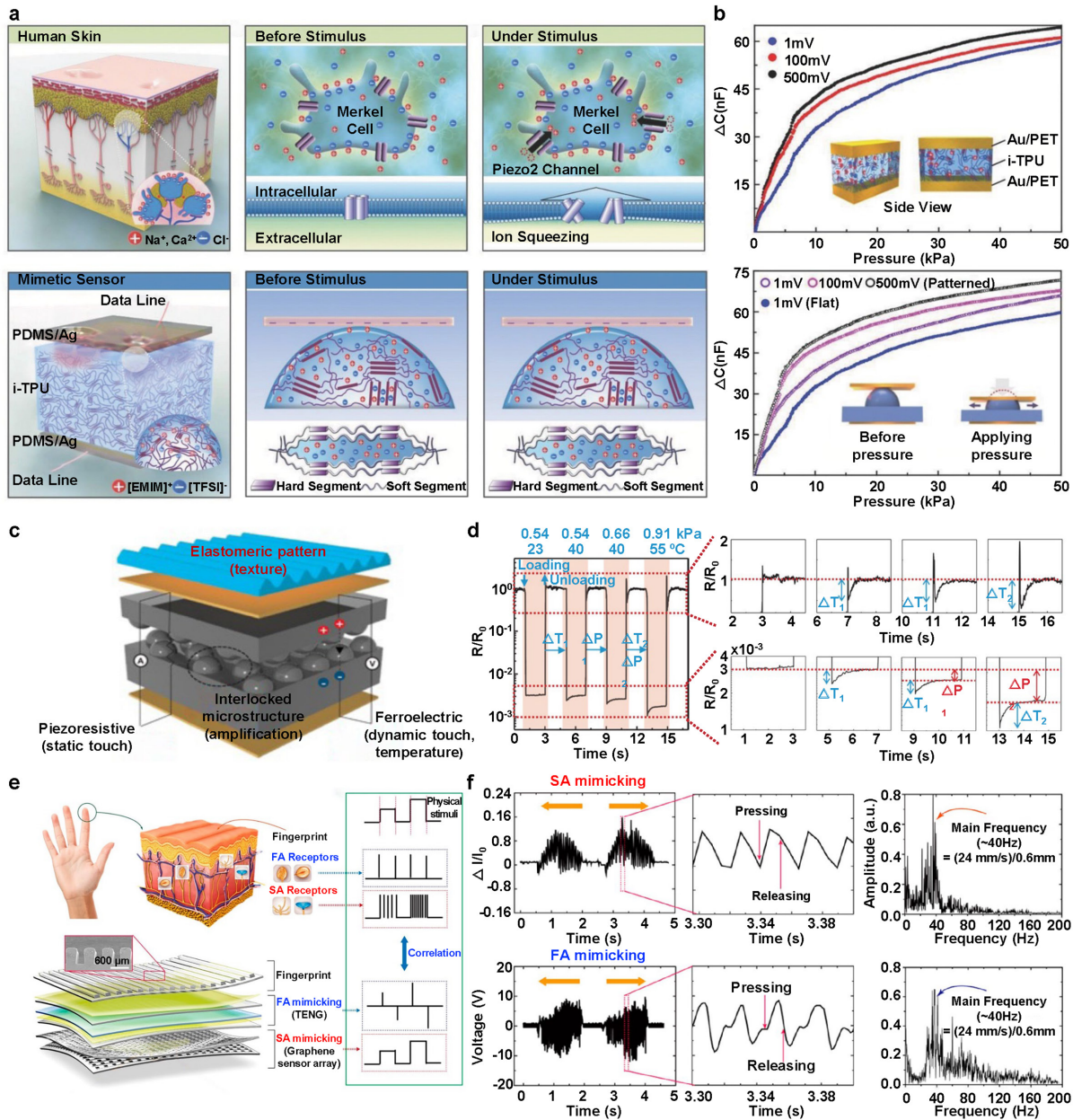


FIG. 3. Human skin-mimicking pressure sensors. (a) Schematic illustration of mammalian mechanosensory units including the Merkel cell mechanoreceptors and design of artificial ionic mechanotransducer composed of i-TPU, silver nanowire electrode embedded in PDMS and wired probes. (b) Capacitive pressure sensing performance of the artificial ionic mechanotransducer using a flat i-TPU film, tested under three different voltage biases. Inset: schematic illustration of the artificial ionic mechanotransducer model system with a flat i-TPU film between Cr (10 nm)/Au (40 nm) electrodes, deposited on PET substrates (top). Capacitive pressure sensing performance of the IMT with a pillar patterned i-TPU film under three kinds of voltage bias. Inset: schematic illustration of the artificial IMT before and after the pressure is applied (bottom). Reprinted with permission from Jin *et al.*, *Adv. Mater.* **29**(13), 1605973 (2017). Copyright 2017 WILEY-VCH Verlag GmbH & Co. KGaA, Weinheim.³⁶ (c) Flexible and multimodal ferroelectric e-skin. The functionalities of human skin are mimicked by elastomeric patterns (texture) and piezoresistive (static pressure), ferroelectric (dynamic pressure and temperature), and interlocked microdome arrays (tactile signal amplification). (d) Variation in relative resistances over time following the loading and unloading cycles of objects at different pressures and temperatures on an interlocked e-skin (left). Magnified variation of relative resistances at the moment of loading/unloading cycles in (left) showing the detection and discrimination of simultaneous temperature and pressure variations (right). Reprinted with permission from Park *et al.*, *Sci. Adv.* **1**(9), e1500661 (2015). Copyright 2015 The Authors.³⁷ (e) Human finger skin and fingerprint structure of epidermis and mechanoreceptors of dermis and schematic illustration of an NTS device (left). Correlation between neural spikes of human skin and electrical output signals of an NTS device for slow and fast adaptation in response to physical stimuli, respectively (right). (f) Texture-dependent electrical and frequency response signals of the SA-mimicking sensor (top) and the FA mimicking sensor (bottom), respectively. The scanning speed is 24 mm/s in both forward and backward directions. Reprinted with permission from Chun *et al.*, *Nano Lett.* **19**(5), 3305–3312 (2019). Copyright 2019 American Chemical Society.⁸⁸

electrical conductivity within the GNP percolation networks. For the FA mimicking sensor, the output signals demonstrated some dependence on pressure, but this was not significant when compared to the SA-mimicking graphene sensor. It is important to note that the TENG was selectively sensitive to vibration inputs rather than pressure, thereby mimicking the FA mechanoreceptors. The frequency responses of the TENG sensor revealed a distinct response curve, which is attributed to the resonance frequency (~ 20 Hz) of the TENG. The functioning of the sensors, which are integrated with a fingerprint structure (FPS), mirrors the human tactile experience via actions such as touching and rubbing the surface of an object [Fig. 3(f)]. When a textured object, marked by its roughness, is rubbed against the periodic FPS design of the sensor at a certain velocity, it leads to the production of electrical signals over time. This is due to the pressure and vibration interaction between the FPS and the textured surface of the object. The sensor that simulates SA mechanoreceptors enhances interactions within the film, while the one mimicking FA mechanoreceptors facilitates the connection of opposing dielectric surfaces in response to the roughness texture. The frequency response was analyzed using Fast Fourier Transform analysis to identify the pattern periodicity, enabling identification of the surface texture. The NTS device, when rubbed over a single-ridge texture at a consistent speed of 24 mm/s, effectively measured the resultant pressure and vibration interactions. The variations in the electrical response caused by sensor contact during scanning at 24 mm/s were distinctly mapped out over time as periodic wave patterns, providing a clear representation of the texture characteristics.

B. Artificial synaptic devices

The human brain is composed of 100×10^9 neurons, and each neuron is connected to 10 000 other neurons, facilitated by a cellular structure called a synapse, allowing advanced computations similar to a supercomputer and being responsible for the storage of memories.^{1–6} The electrical signal associated with sensory information is transmitted to the next neuron by the chemical diffusion of various neurotransmitters (Na^+ , Ca^{2+} , K^+ , etc.) in the synaptic vesicles, and the neurotransmitter receptors decode the transmitted neurotransmitters. In this process, the quantity and type of neurotransmitter released are decoded into the electrical signal format to be propagated in the neuron. There are two types of plasticity in synapses that link neurons together; short-term plasticity which temporarily stores information and long-term plasticity which stores information for a relatively longer period. Each type of plasticity is divided into short-term potentiation (STP), short-term depression (STD), long-term potentiation (LTP), and long-term depression (LTD). Potentiation results in an increase in synaptic strength due to repeated synapse stimulation,

while depression leads to a decrease in synaptic strength. Therefore, before the recognition of information occurs in the brain, a preprocessing of information at the synapse allowing the brain to efficiently recognize a vast amount of information with a limited number of neurons. In the case of tactile sensation, various types of tactile sensations from different locations, each with varying intensities, are transmitted to the brain, forming an extensive information base for recognition. Therefore, in the biomimicry of the tactile sensory system, artificial synapses play a pivotal role. Two-terminal artificial synapse and three-terminal artificial synapse are the two representative types of artificial synapse design (Table III). A prominent approach for realizing a two-terminal artificial synapse involves applying an electrical signal to the electrodes, inducing the characteristic modulation of the insulator between the electrodes.^{89–91} Representative methods for implementing this type of synapse include the use of resistive random-access memory (RRAM),^{92–94} magnetic random-access memories,^{95–97} and phase-change memories.^{98–101} With the additional electrode to control the characteristics of the insulator, a three-terminal transistor for biomimicry of artificial synapse can be designed.^{50,102–105} Ferroelectric field-effect transistors, floating gate field-effect transistors, and optoelectronic field-effect transistors are representative examples of three-terminal artificial synapse design. In the case of a two-terminal artificial synapse, the characteristics of the insulator between the two electrodes change according to the electrical signal applied to the electrodes, which allows the limited information (high or low) that can be expressed with a single artificial synapse. However, it can retain information without supplied power, which indicates a nonvolatile memory characteristic. For the transistor-based three-terminal artificial synapse, a constant power supply is essential for storing information, as it controls information storage with the electrical signal applied to the gate of the transistor. However, it has the advantage of a wide information expression with a single three-terminal artificial synapse, such as controlling the intensity of the output signal or regulating the synaptic weight via short-term plasticity and long-term plasticity adjustments.

In the RRAM, which is widely used type for a two-terminal artificial synapse, the application of electrical stimuli to the two electrodes induces a change in the properties of the dielectric, modulating the output resistance into either a high or low state. The modulated output resistance state is maintained even in the absence of a supply voltage. Kim *et al.* introduced the neuromorphic sensory system inspired by the golden tortoise beetle (*Charidotella sexpunctata*), which converts the applied pressure into a voltage pulse signal with a capacitance-based tactile sensor and activates the corresponding quantum-dot light-emitting diode (QLED) array with the tactile information stored in an RRAM array.¹⁵ The LTP and LTD characteristics of biological

TABLE III. Properties of artificial synapse: two-terminal artificial synapse and three-terminal artificial synapse.

	Number of electrodes	Memory type	Representative types
Two-terminal artificial synapse	2	Nonvolatile	Memristor (RRAM), magnetic random access memories, phase-change memories)
Three-terminal artificial synapse	3	Volatile	Transistor (ferroelectric field effect transistor, floating gate field effect transistors, optoelectronic field effect transistor)

synapse have been biomimicked through RRAM. The transition metal oxide TiO_2 is used as the dielectric material for RRAM [Fig. 4(a)].^{106,107} Current flows along the oxygen vacancy pathway in the TiO_2 . Initially, the distribution of oxygen vacancies is uneven, but when a voltage is applied, oxygen vacancies with a positive charge diffuse to the other side of the electrode, creating a current pathway and inducing a low-resistance state (LRS) for TiO_2 . Applying an opposite voltage causes the shifting of oxygen vacancies to the initial state,

disrupting the current pathway and resulting in a high-resistance state (HRS) [Fig. 4(b)]. During this process, oxygen vacancies attempt to return to their original positions for thermodynamic stability; but an infinitely extended duration is required, contributing to the nonvolatile characteristic of RRAM. Utilizing the shifting of oxygen vacancies in response to voltage enables the control of the resistance state RRAM (LRS or HRS), ultimately facilitating data storage in a manner analogous to the representation of logic circuit values, namely, 0 and 1.

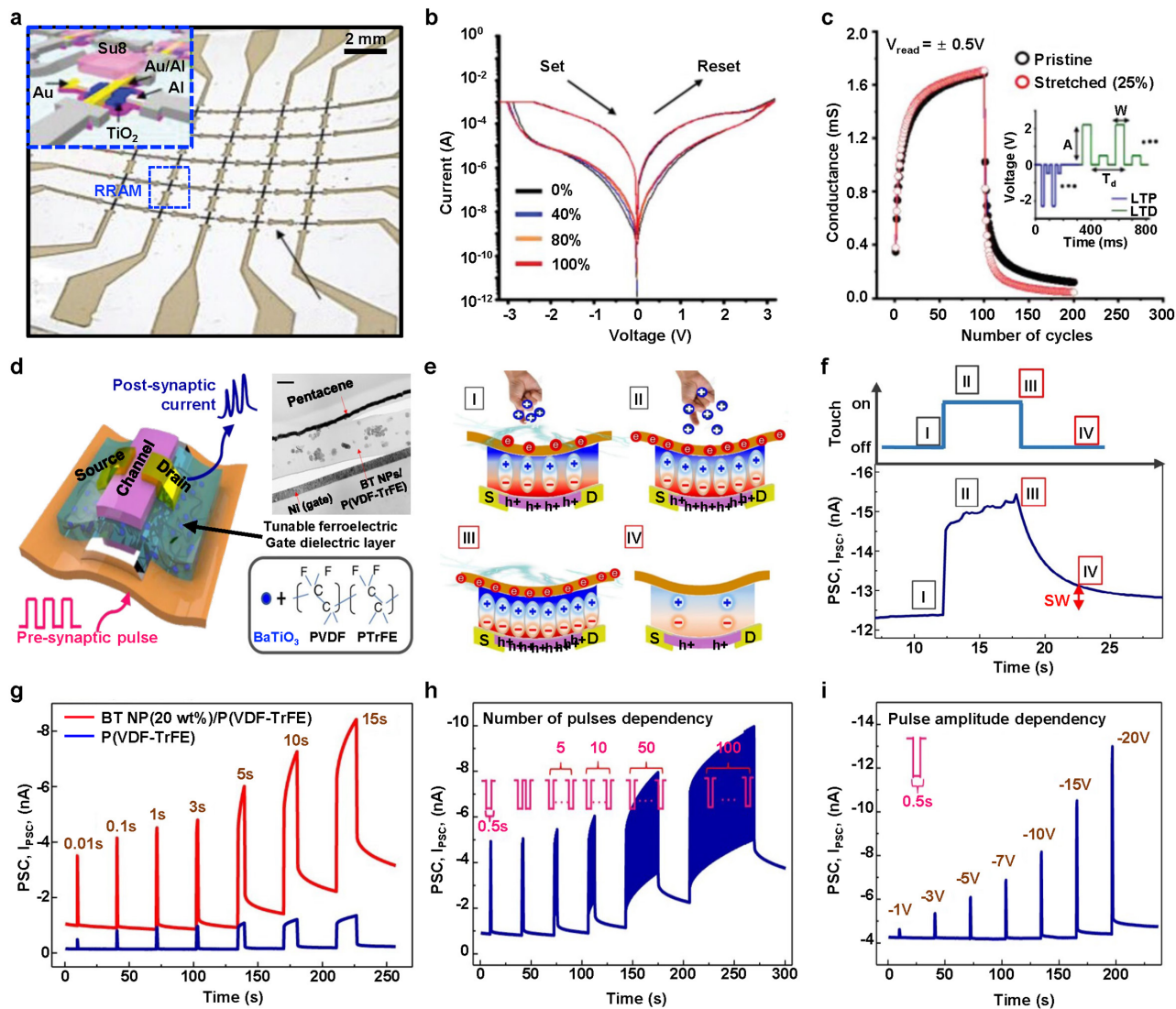


FIG. 4. Artificial synaptic devices. (a) Photograph image of the RRAM based stretchable artificial synapse. The inset illustrates the structure of the RRAM, comprising transitional TiO_2 and electrodes positioned on the island structure, encapsulated with SU-8. (b) Electrical properties of the stretched RRAM with different strains from 40% to 100%. (c) The LTD and LTP characteristics of the fabricated artificial synapse in original state (black) and elongated state (red). Reprinted with permission from Kim *et al.*, *Adv. Mater.* **33**(44), 2104690 (2021). Copyright 2021 Wiley-VCH GmbH.¹⁵ (d) A schematic image of Fe-OFET based artificial synapse. Inset shows the focused ion beam (FIB) image of fabricated Fe-OFET (Scale bar = 200 nm). (e) and (f) Schematics of dipole reorganization process in ferroelectric layer of the Fe-OFET during tactile stimulation process ($\sim 0.3 \text{ kPa}$) (e) and the corresponding PSC output result (f). (g)-(i) The output characteristics of PSCs using different ferroelectric materials [BT NP (20 wt. %)/P(VDF-TrFE) and P(VDF-TrFE)] (g), their dependency based on the number of applied pulses (h), and their reliance on different applied pulse amplitudes (i). Reprinted with permission from Lee *et al.*, *Nat. Commun.* **11**(1), 2753 (2020). Copyright 2020 The Authors.

TiO₂-based RRAM possesses the important characteristics of LTP and LTD found in synapses. When the RRAM was excited with -2.3 V at 20 ms intervals for 100 times, it was observed that the conductance increased with the number of excitations, similar to the characteristics of LTP. Subsequently, when inhibited with 2.2 V at 100 ms intervals for another 100 times, the conductance decreased as the number of inhibitions increased, similar to the characteristics of LTD. In addition, the LTP and LTD characteristics of RRAM showed similar result when RRAM is stretched for 25% [Fig. 4(c)]. The property of RRAM was maintained after 1000-times repeated cyclic stretching (25%), enabled by the implementation of a polyimide island structure on a stretchable substrate, along with the use of conductive ink for metal interconnection, which improved contact resistance by applying an Al/Au electrode. Therefore, this TiO₂-based stretchable RRAM is progressive because it biomimics the LTP/LTD characteristics of biological synapses based on stretchable RRAM and maintains high performance even under physical deformations (25% stretching) which is important in wearable electronics.

Figure 4(d) shows a ferroelectric organic field-effect transistor (Fe-OFET)-based three-electrode artificial synapse. Inspired by the piezo-2 channel in Merkel cells, a triboelectric-capacitive coupled tactile sensor is designed to convert the applied pressure into an electrical potential signal and transmit to the Fe-OFET artificial synapse.¹⁶ The Fe-OFET artificial synapse can handle complex sensory process internally, reducing the processing burden on external systems and enhancing overall system efficiency and responsiveness. When the electrical potential signal, converted from the pressure signal (presynaptic pulse), is applied to the gate of the Fe-OFET, the dipole directions of the gate, composed of ferroelectric materials, barium titanate nanoparticles (BT NPs) and poly(vinylidene difluoride-trifluoroethylene) [P(VDF-TrFE)], undergo a change in ferroelectric properties,^{108–110} which induces the output current [post-synaptic current (PSC)] in the form of a paired pulse signal. When a negative voltage is applied to the gate of the Fe-OFET, the initially random distribution of dipoles, the direction of the dipoles becomes uniform, with the negative dipole facing up, resulting in an increase in PSC. When a positive voltage is applied to the gate of Fe-OFET, the dipoles are positioned opposite (negative dipole facing down) compared to the negative voltage applied, leading to a decrement in PSC. If the applied gate voltage diminishes, the polarization direction gradually undergoes random changes, causing the previously increased or decreased PSC to return to its initial value [Figs. 4(e) and 4(f)]. By adjusting the retention time of the pulse applied to the gate, the synaptic weight can be modulated. When the applied pulse voltage has a frequency of 0.1 Hz , the peak PSC reaches -6 nA and stably decays to -2 nA after $\sim 5\text{ s}$, demonstrating STP characteristic. By contrast, with an applied pulse voltage frequency of 1.42 Hz , LTP characteristics are observed [Fig. 4(g)]. These characteristics indicate that as the frequency of the applied pulse signal increases, the PSC shows more LTP characteristics. Furthermore, as the intensity of the applied pulse and the number of pulses increases, the PSC characteristics become more indicative of LTP [Figs. 4(h) and 4(i)]. After a cyclic bending test with 100 000 cycles of 1.25% strain applied, the paired pulse ratio (PPR; 2^{nd} peak current value/ 1^{st} peak current value) of PSC which has paired pulse signal output from Fe-OFET artificial synapse showed negligible value of less than 0.1. Furthermore, both PPR and synaptic weight exhibited minimal changes, with a maximum alteration of up to 1.88% strain,

indicating no significant degradation in performance. Similar to actual biological memory, the Fe-OFET artificial synapse exhibits strength, and with repeated stimuli, it shows an increase in the decay time of PSC, indicating LTP characteristics. A process for temporal data storing or processing data are important for recognizing enormous amounts of information efficiently. Although the performance of miniaturized central processing units (CPUs) (e.g., MCUs) has been improved due to recent technological advancements, there are still limitations in data processing speed and capacity. Therefore, the concept of an artificial synapse, capable of pre-processing pressure signals beyond simply detecting pressure, highlights significant importance as it supports smoother and more efficient data processing.

C. Artificial neuromorphic systems for the recognition of tactile information

Inspired by the biological tactile sensory system, software algorithm-based computation has given rise to artificial tactile systems that biomimic the complex characteristics of human touch.^{111–116} Unlike traditional sensors, which often provide binary responses to stimuli, neuromorphic artificial tactile sensory systems embed the principles of neural computation in tactile sensors with learning capabilities, enabling them to dynamically interact with varying environmental conditions and stimulus. In the pursuit of biomimicry of human tactile sensory system, recent studies on artificial tactile sensory systems have delved into the integration of neural network models within neuromorphic devices.^{117–121} This innovative approach marks a transformative shift, enabling tactile sensors not to merely respond to stimuli but to process and interpret sensory information similar to the sophisticated human nervous system.

Figure 5(a) depicts the neuromorphic artificial tactile system that biomimics the human tactile sensation.¹⁷ TENG enables the generation of a current when an external pressure is applied, indicating that no external power source is required.^{122–127} The output current generated by the TENG under the externally applied pressure is connected to the collector of a bipolar junction transistor (BJT), which has a single-transistor latch (STL) structure.^{128,129} In the STL structure, with an increase in the current generated by the TENG, which is connected to the collector of STL, electrons from the emitter, which is grounded, move toward the base, generating electron-hole pairs. The generated holes are accumulated in the floated base, which reduces the potential barrier between the emitter and base, inducing an increased supply of electrons to the base, and more holes generated by electron-hole pairs are accumulated in the base as a positive feedback. The voltage difference between the collector and base when a specific current from the TENG initiates the positive feedback is referred to as the latch-up voltage. When the voltage between the collector and base is less than the latch-up voltage, the STL maintains the HRS state, while exceeding the latch-up voltage causes the STL to transition to LRS [Fig. 5(b)]. With the attachment of a parasitic capacitor to the collector and ground of the STL, the discharge and recharge effects of the capacitor lead to a continuous discharge until it reaches the threshold voltage (VT) of the STL. Once VT is reached, the catastrophically increased current charges the capacitor, and the output voltage decreases. This discharge and recharge of the parasitic capacitor result in spikes in the output of the STL. As shown in Figs. 5(c) and 5(d), under a gradual increase in the intensity of applied pressure to the TENG (output current of the TENG increases), after the output voltage of the STL exceeds the latch-

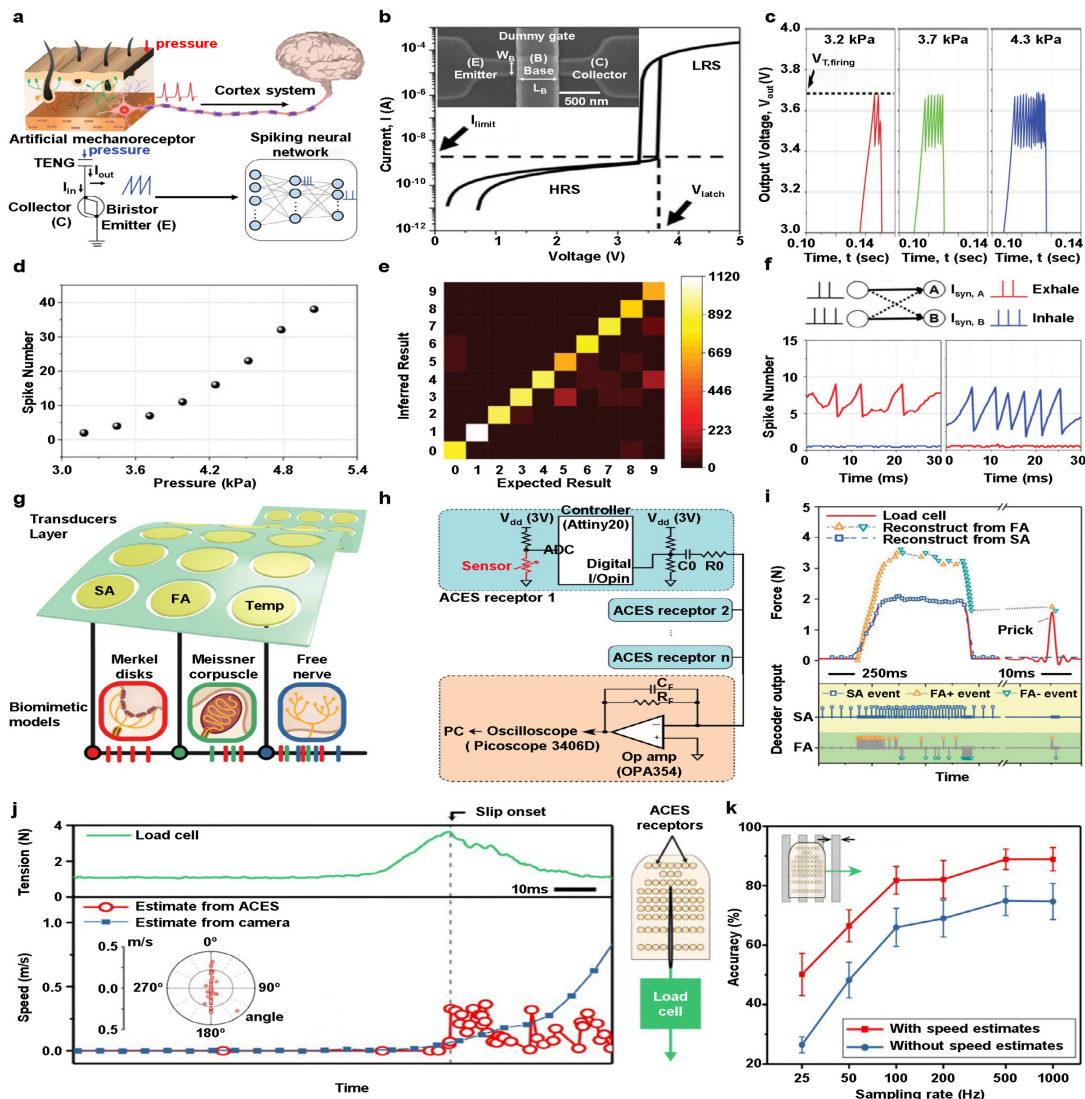


FIG. 5. Artificial neuromorphic systems for the recognition of tactile information. (a) A schematic of the biological and artificial tactile sensation system. Mechanoreceptors produce spike signals upon detecting the pressure (frequency of spike increases with respect to the intensity of applied pressure) and transmit these signals to the cortex for tactile recognition. Mimicking the biological tactile sensation mechanism, TENG generate the current when pressure is applied and converted into spike signal by biristor neuron and the spike signal based tactile information is recognized with SNN. (b) Scanning electron microscopy (SEM) image of fabricated biristor neuron with STL structure. (c) Spiking properties of biristor neurons with different applied pressures to TENG. (d) The number of spike characteristics with respect to different intensity of applied pressure. (e) Confusion matrix of MNIST handwritten digit pattern with accuracy of 85.8%. (f) Demonstration of breathing classification with fabricated artificial tactile sensory system. The results indicate successful recognition of inhale and exhale. Reprinted with permission from Han *et al.*, *Adv. Sci.* 9(9), 2105076 (2022). Copyright 2022 The Authors.¹⁷ (g) A schematic illustration of multimodal ACES array which sense the applied pressure and temperature with multiple spatially distributed sensor. (h) Block diagram of ACES where multiple spatially distributed sensors (blue) are connected to the operational amplifier-based decoder (orange). (i) Estimated intensity of applied force sensed by FA and SA receptors (top). The output responses from decoder (bottom). (j) Comparison of estimated movement of pulled out needle by ACES (red) and camera (blue). Bottom graph demonstrates the estimated movement (red dot lines) and direction (red dots in circle inset) of pulled out needle from ACES. (k) Estimated movement accuracy detected with ACES with different sampling rate. Reprinted with permission from Lee *et al.*, *Sci. Rob.* 4(32), eaax2198 (2019). Copyright 2019 The Authors.¹⁸

up voltage, the output spike frequency of the STL increases. The handwritten digit [Modified National Institute of Standards and Technology (MNIST) database] recognition simulation based on a three-layer SNN showed a high recognition rate with 85.8% accuracy. The handwritten digit recognition is based on the open-source code

SNN released by Duan *et al.*¹³⁰ and consists of 784 artificial mechanoreceptors representing pixels in a 28×28 array, which recognize the number of spikes according to pressure. It then passes through a hidden layer of 100 neurons to 10 output neurons representing the digits 0 to 9. In addition, with the two types of TENG sensors (bending- and

wind-type mechanoreceptor sensors) connected to independent STLs, breathing type (inhale or exhale) determination was demonstrated. The bending-type mechanoreceptor sensor senses the movement of the abdomen, and the wind-type mechanoreceptor sensor senses the air flow from the nose. Using these two types of sensors, the changes in the frequency values of the output STL during exhaling and inhaling were translated into synaptic weights by adapting the threshold voltage and conductance of the STL-based synapse. With the simulated three-layer SNN, breath recognition, i.e., whether the current state is inhaling or exhaling, was realized with high accuracy.

Humans can recognize the intensity and location of an externally applied pressure because of numerous mechanoreceptor cells located in the skin. The complex computation related to the tactile information is achievable with a limited number of neurons because the nerve connected to the somatosensory cortex is composed of nerve fibers, and each fiber is composed of numerous neurons that are connected to the mechanoreceptor cells. Moreover, because spikes are transformed into a single spatiotemporal pattern in the form of action potentials, the latency depends on the speed of action potential propagation, not on the number of receptors.^{131–133} Figures 5(g) and 5(h) depict an asynchronously coded electronic skin (ACES) with a single conductor for signal processing employed to transmit tactile signals detected by multiple spatially distributed sensors inspired by the human tactile sensory system. The sensor is composed of a temperature sensor and tactile sensors, which can monitor the SA and FA pressures. After sensing the applied pressure, the signals are transmitted to a decoder, which decodes the transmitted signal in the form of a single integrated spatiotemporal signal [Fig. 5(i)]. A spiking convolutional network processes the decoded single spatiotemporal signal for recognition, allowing the prediction of the movement associated with the applied pressure. The spiking convolutional network from event-based optical flow algorithm reported by Benosman *et al.* is implemented to ACES for predicting the movement.¹³⁴ When the movement is detected from one receptor at time t_0 , the system checks for prior movement from nearby receptors, recognizing the moment distance D , and calculates the movement magnitude ($\frac{D}{t_0 - t_{prior}}$). The direction of distance D between the prior movement and current movement is calculated by $a \tan 2(dx, dy)$ where d_x and d_y represent the x axis and y axis components of D . Subsequently, the movement magnitude and direction are averaged for predicting future movement. Accordingly, rapid slip detection with proposed tactile sensory system was demonstrated, revealing faster estimation time compared to the movement estimation by vision recognition. Because the recognition accuracy of the human nervous system is closely related to the propagation time of action potentials as shown in Fig. 5(k), the movement prediction accuracy improves with an increase in the sampling rate. Another advantage of ACES is its robustness to damage. Unlike conventional multiplexing arrays that connect each array cell through column lines and row lines, ACES connects each array cell to a single planar conductive substrate, ensuring that each receptor and the conductive substrate are physically connected. Therefore, even if parts of the substrate are damaged (mechanically cut), as long as the conductive pathway is not completely damaged, the ACES can continue to measure pressure and temperature signals. This capability is possible because ACES analyzes the signals detected from each FA, SA, and temperature sensors through a decoder as a single integrated spatiotemporal signal. By biomimicking the human tactile sensory system, which integrates signals

from mechanoreceptor cells into a single spatiotemporal signal, the proposed system can be scaled up to 10 000 independent sensors.

D. Integrated neuromorphic tactile sensory systems for biomimicry of afferent and efferent neuron functions

Tactile sensory systems convert pressure sensed in the skin into action potentials, which are pulse-shaped signals based on frequency.^{135–139} These signals are then transmitted through the nervous system to the somatosensory cortex, and by stimulating motor neurons through the motor cortex, muscle movements are produced for the necessary movements. Currently, several studies have focused on biomimicking such tactile sensory systems to recognize externally applied pressure, convert it, and stimulate nerves accordingly.^{19–22,140–143}

Figure 6(a) shows an artificial tactile sensory system, which is composed of a tactile sensor, organic ring oscillator, and an artificial synaptic transistor.¹⁹ The resistance-based tactile sensor converts the applied pressure signal into resistance, and a frequency-based pulse signal is generated by organic transistors. Subsequently, ion gel-based metal-oxide semiconductor FETs (MOSFETs), which biomimic a synapse, convert the voltage-based pulse signal into a current-based pulse signal to stimulate nerves confirmed by the movement of cockroach legs. For the pressure sensor, a pyramid structure coated with carbon nanotubes (CNTs) is employed. When pressure ranging from 0 to 90 kPa is applied, the contact area with the electrode beneath the pyramid structure changes, resulting in an increase in resistance as the intensity of applied pressure increases. This structure is designed to convert the resistance variations, modulated by a voltage-dividing configuration, into a voltage signal corresponding to the applied pressure [Fig. 6(b)]. The organic ring oscillator is designed to have an odd number of inverters for the modulation of a DC voltage into a frequency-based pulse signal, while the single inverter is composed of a pseudo-complementary metal-oxide semiconductor (CMOS).^{144–147} When the applied DC voltage increases, the output frequency and peak voltage of the organic ring oscillator output increase [Fig. 6(c)]. Then, with the ion-gel MOSFET-based synapse, the voltage-based pulse signal is converted into a current-based pulse signal. While the frequency of the current-based pulse has a frequency similar to that of the voltage-based pulse, the peak current exhibits a more linear response to pressure compared to the signal transformed by the organic ring oscillator [Fig. 6(d)]. By stimulating the nerve related to the legs of a cockroach, the tactile sensation and signal modulation were successfully demonstrated.

Furthermore, simultaneous sensing of pressure and temperature was achieved by neuromorphic sensorimotor loop embodied electronic skin (e-skin), with the signals converted to stimulate the sciatic nerve associated with leg muscles [Fig. 6(e)].²⁰ The outputs of the resistance-based pressure sensor and temperature sensor are each transformed into voltage signals and further converted into pulse signals by ring oscillators and edge detectors. For the distinction of converted signals, the pressure sensor is connected to a ring oscillator composed of seven pseudo-CMOSSs, while the temperature sensor is connected to a ring oscillator with five pseudo-CMOSSs. Compared to previous research, the pseudo-CMOS is designed with a MOSFET gate composed of a high- k trilayer dielectric (nitrile butadiene rubber; $k \sim 28$, nonpolar poly(styreneethylene-butylene-styrene); $k \sim 2.4$, octadecyltrimethoxysilane),^{148–152} aiming to achieve high charge-carrier mobility. This design enables the maintenance of a low driving voltage while

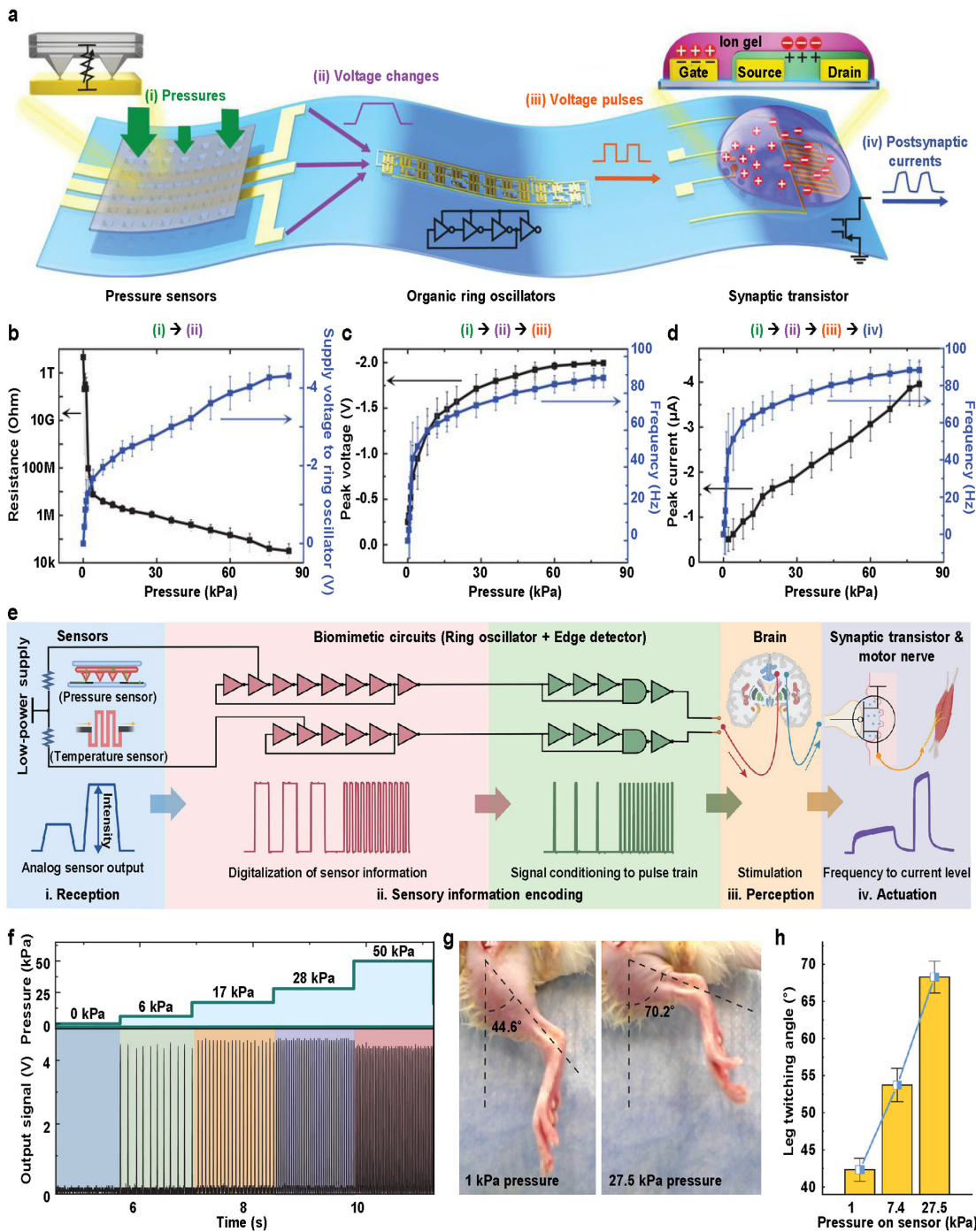


FIG. 6. Biomimic artificial tactile sensation system. (a) A schematic illustration of biomimic artificial tactile sensory system composed of pressure sensor, organic material-based ring oscillator and artificial synaptic transistor. (b) Resistance output from pressure sensor with respect to different applied pressure. (c) Peak voltage and frequency responses of converted pressure stimuli from organic material-based ring oscillator. (d) Peak current and frequency responses from artificial synaptic transistor according to the applied pressure. Reprinted with permission from Kim et al., *Science* **360**(6392), 998–1003 (2018). Copyright 2018 The Authors.¹⁹ (e) A schematic illustration of neuromorphic sensorimotor loop embodied e-skin. (f) Pulse train output of neuromorphic sensorimotor loop embodied e-skin when applied with different intensity of pressure. (g) Photographic images of leg movements using a neuromorphic sensorimotor loop embodied e-skin under varying pressure intensities. (h) Leg twitching angle difference according to the different intensity of applied pressure. Data points represent average values from four rats. All error bars refer to standard deviations. Reprinted with permission from Wang et al., *Science* **380**(6646), 735–742 (2023). Copyright 2023 The Authors.²⁰

significantly improving carrier mobility. The frequency-based pulse transformed by the ring oscillator is further refined using an edge detector constructed with a delay network and an AND gate [Fig. 6(f)]. This mechanism captures the rising edges in the pulse signal, enhancing it into a sharper and more defined waveform. The output signal from the edge detector is further converted into a current pulse by the synaptic transistor. In contrast to previous research, a stable ionic dielectric was formed by blending an ionic conducting elastomer and polyelectrolyte {poly[(1-vinyl-3-propyl-imidazolium) bis (trifluoromethanesulfonyl)imide]}. The polyelectrolyte was securely anchored in the ionic conducting elastomer, exhibiting minimized influence from biofluids, ensuring stable operation after implantation. For the transistor that compose the ring oscillator and edge detector, all materials comprising the substrate (PDMS), semiconductor (CONPHINE¹⁵³), interconnect (CNT), and dielectric layer (high-k tri-layer dielectric) are stretchable. Therefore, even after conducting 1000 cycles of cyclic stretching tests with 60% applied strain, there was no performance degradation indicating reliability of the stretchable device. Figures 6(g) and 6(h) show the sciatic nerve stimulation after the implantation of the proposed system. The applied pressure signal is effectively transformed into a current-based pulse signal, eliciting stimulation of the sciatic nerve under varying pressure intensities. The e-skin system is monolithically integrated by combining all electrical and mechanical features within a single stretchable device platform without any rigid components. This integration simplifies the structure, reduces weight, and enhances the flexibility and stretchability of the e-skin. The key advantages of the e-skin include its low driving voltage (± 0.75 V) and low power consumption (0.25 pW). Featuring a stretchable trilayer dielectric layer with a low subthreshold swing value and high mobility, the e-skin can successfully output pulse-train signals across various frequencies, driven by ± 0.75 V. This driving voltage is significantly lower than that of typical stretchable electronics, enhancing its efficiency and applicability.

In cases of severe skin damage resulting in permanent impairment of tactile function, it is crucial to not only substitute the tactile sensation but also accelerate the wound healing process of damaged skin. In addition, because the implantable device is implanted into the body, which has considerable moisture, moisture resistance is important for stable long-term operation. Therefore, for the fundamental solution for treating severely damaged skin with impaired tactile function, a skin-regenerative, tactile-function-replaceable, and moisture-resistant integrated system is needed. Figure 7(a) depicts an implantable and long-term operable wirelessly powered tactile sensory system-embedded artificial skin (WTSA).²¹ This system aims to restore permanently impaired tactile function and expedite the wound regeneration process of severely damaged skin. The WTSA comprises an artificial skin that biomimics the extracellular matrix to facilitate layer-by-layer skin regeneration, a tactile sensor for the recognition of externally applied pressure intensity, a wirelessly powered pressure-frequency modulation module (WPPFM) circuit, conductive hydrogel-coated neural interface to minimize fibrosis formation for effective nerve stimulation,¹⁵⁴ and encapsulation with multiple layers for prolonged operation duration. The artificial skin within the WTSA, composed of a hydrogel mixture containing fibrin and collagen, creates a microenvironment resembling the extracellular matrix of human skin.^{155–157} This facilitates the regeneration process of severely damaged skin, accelerating layer-by-layer skin regeneration. The

sophisticated single integrated system biomimic the tactile sensing mechanism by converting the intensity of applied pressure measured through tactile sensor which is embedded in artificial skin to frequency-based sawtooth pulse signal and is capable of stimulating the sciatic nerve with conductive gelatin coated nerve interface which minimize the foreign body reaction enabling stable long-term electrical stimulation. In addition, quantitative analysis of leg movement and corresponding electromyogram (EMG) signals was conducted to validate the successful operation of the advanced artificial sensory system in response to varying pressure intensities [Fig. 7(b)]. The varying leg movements in response to applied pressures, when an external pressure is recognized and converted into action potential mimic electrical signal to stimulate the sciatic nerve through a single integrated system, characterize the features of a neuromorphic sensory system. Unlike previous studies that primarily focused on tactile sensory restoration, the WTSA accelerates layer-by-layer skin regeneration while minimizing scar formation and substitutes the permanently impaired tactile sensation simultaneously. The fibrosis formation between the neural interface and sciatic nerve disrupts effective long-term electrical stimulation; it is mitigated by precisely controlling the modulus of the conductive hydrogel, which is coated on the neural electrodes to minimize the mechanical difference between the nerve and conductive hydrogel-coated neural interface. For implantable systems that operate inside the body, moisture resistance is a crucial property. Therefore, in this study, the system is protected from biofluids through multi-layer encapsulation (PDMS/Parylene C/Al₂O₃), and the components of the tactile signal processing is composed of inorganic materials which are not vulnerable to moisture. The PBS acceleration test showed no performance degradation until 429 days at 37°C, which is calculated by Arrhenius equation indicating outstanding encapsulation property. These properties ensure the stable long-term operation of the WTSA after implantation. This integrated platform presents a new approach for accelerate the skin regeneration and replacing the permanently dysfunctional tactile sensory simultaneously. The WTSA successfully demonstrated the *in vivo* experiment with severe skin damaged rat presenting the accelerated skin regeneration and the precisely analyzed the leg movement by measuring EMG signals as well as the leg angle movement while different intensity of external pressure is applied to severely damaged skin. The WTSA is highlighted by showing the potential to be applied from basic research to clinical research in biomedical field and associated studies.

Figure 7(c) depicts an artificial neural tactile sensing system with an FA- and SA-integrated tactile sensor.²² Biomimicking the actual skin composed of FA and SA mechanoreceptors, an integrated tactile sensor was fabricated by adjusting the ratio of rGO to emulate FA and SA characteristics. BaTiO₃ is a representative material with piezoelectric properties, and when it is mixed with rGO, a specific ratio beyond the percolation threshold (0.5%) leads to the interconnection of neighboring rGO, providing piezoresistive characteristics. For the piezoelectric property of the FA sensor, which is designed to monitor subtle movements such as vibrations, the mixing ratio of rGO and BaTiO₃ is controlled to be below the percolation threshold. By contrast, in the SA sensor, which is designed to monitor the intensity of applied pressure, a piezoresistive characteristic is achieved by increasing the amount of rGO in conjunction with. Under 10 000 repeated pressure application cycles, both sensors exhibited no performance degradation [Fig. 7(d)]. By the signal conversion process, the signals are transformed into spike

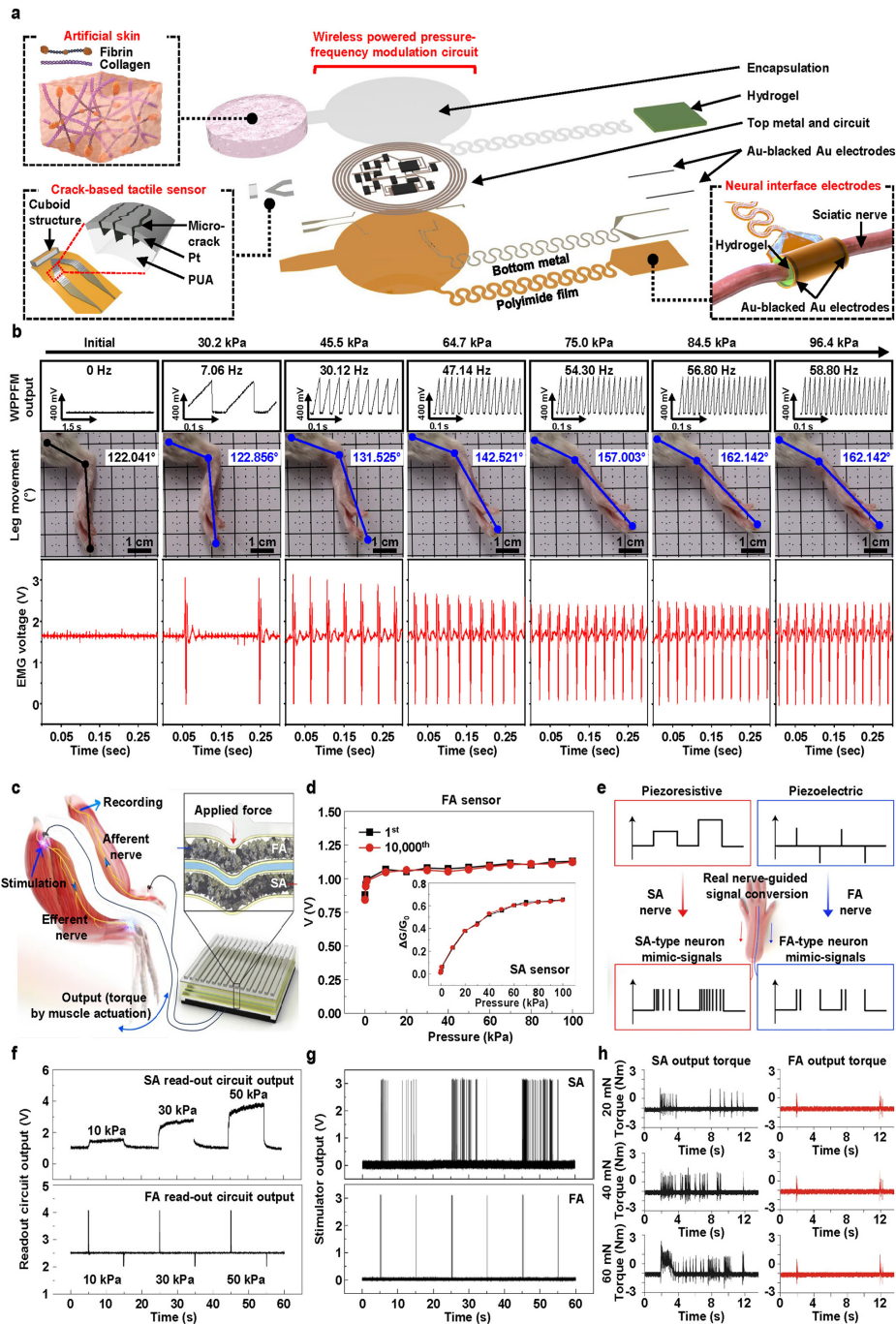


FIG. 7. Neuromorphic tactile sensory systems for biomimicry of afferent and efferent neuron functions. (a) A schematic illustration of WTSA composed of artificial skin, crack-based tactile sensor, WPPFM circuit, conductive gelatin coated neural interface electrodes to minimize fibrosis occurring. (b) An analysis of leg movement angle difference (blue) and corresponding EMG signal (red) while stimulated with converted signal from WPPFM (black) under different pressure is applied. (c) A schematic illustration of artificial neural tactile sensing system with FA- and SA-integrated tactile sensor. (d) Characteristics of FA and SA sensor (inset) under different intensity of applied pressure (0.1–100 kPa) measured with 10 000 repeated times. Reprinted with permission from Kang *et al.*, Nat. Commun. 15(1), 10 (2024). Copyright 2024, The Authors.²¹ (e) Biomimicry of SA- and FA-type mechanoreceptors with distinct spike signal outputs according to applied pressure. (f) Characteristics of SA and FA sensors output under different intensity of applied pressure. (g) SA and FA neural stimulator outputs of converted signal from SA and FA sensors. (h) *In vivo* demonstration of the artificial neural tactile sensing system with FA- and SA-integrated tactile sensor by measuring the amplitude of torque from leg movement while applying static pressure (20, 40, and 60 mN) to SA and FA sensors. Reprinted with permission from Chun *et al.*, Nat. Electron. 4(6), 429–438 (2021). Copyright 2021 The Author(s) under exclusive license to Springer Nature Limited.²²

shapes. The FA sensor forms spikes at the moment of pressure application and release, while the SA sensor, during sustained pressure, exhibits continuous spikes with different frequencies according to the intensity of applied pressure [Figs. 7(e)–7(g)]. Stimulation of the efferent nerves with converted spike-based signals and measuring the resulting torque values for leg movement indicated that the leg moved in accordance with the characteristics of SA signals, where spikes occurred at the onset and release of applied pressure. Similarly, sustained pressure led to leg movements characterized by varying torque intensities, aligning with the FA signals [Fig. 7(h)]. This demonstrates the feasibility of nerve stimulation by SA and FA characteristics. In addition, by mimicking the actual fingerprints with the FA- and SA-integrated tactile sensor, the system was trained with the signals using a deep-learning algorithm to recognize fabric textures. The 20 different fabric textures were trained and tested by the fingerprint mimic FA- and SA-integrated tactile sensor by rubbing the fabric samples on the integrated sensor. By using the moving-average method, the background bias signal which dominantly contributes to noise, is removed from the collected data followed by discrete-time Fourier transform step. The texture features from collected data are extracted with power spectral density (PSD) analysis. The collected data were trained and tested by deep learning algorithm (Neural Network Pattern Recognition Toolbox from MATLAB version 2017b). The FA signal alone achieved an accuracy of 96.8%, the SA signal alone achieved 96.2% accuracy, and when both FA and SA signals were considered, an exceptionally high accuracy of 98.8% was achieved. This novel system features sensors that can mimic human SA and FA mechanoreceptors by controlling the ratio of rGO to BaTiO₃, allowing it to selectively and sensitively detect both pressure and vibration. After sensing the externally applied pressure, the system can generate sensory neuron-like signals that mimic real tactile nerve signals as the neuromorphic system. This is critical for applications where an accurate replication of human tactile sensing is required, such as in prosthetics or humanoid robotics. Another strength of the system is that it is capable of learning to classify fine and complex textures using deep learning techniques, enhancing its utility in practical applications by enabling it to interact intelligently with various surfaces and textures.

IV. CONCLUSION AND FUTURE PERSPECTIVES

The exploration of the human nervous system and the development of neuromorphic devices designed to emulate its complex functionalities have marked significant milestones in the realm of biomedical engineering and neurotechnology. With the ability of the human nervous system to process information via 100×10^9 neurons, recent advancements have focused on creating artificial tactile sensory systems that closely mimic the tactile perception mechanisms found in humans. These systems, which employ various transduction methods and materials, have shown promise in enhancing human-machine interactions and providing solutions for individuals with impaired tactile sensation due to skin-related diseases.

The integration of tactile sensors that replicate the functionality of mechanoreceptors into neuromorphic devices has paved the way for the development of sophisticated artificial skins and other human-centric devices. These innovations not only offer the potential to restore tactile sensation but also contribute to the advancement of intelligent robotics and prosthetics, improving the quality of life for those affected by sensory loss. Furthermore, the incorporation of artificial synapses and neural networks into these systems highlights the

ongoing efforts to achieve a deeper understanding and replication of human sensory and neural processes.

Moving forward, the field of neuromorphic engineering evidently holds vast potential for breakthroughs in artificial perception systems. Continued interdisciplinary research is essential to overcome existing challenges and expand the capabilities of neuromorphic devices. This includes enhancing the scalability, stability, and accuracy of these systems as well as developing new materials and fabrication methods to further mimic the intricacies of human tactile sensation. Ultimately, the convergence of neuroscience, materials science, and electronic engineering in neuromorphic device development promises to revolutionize the approach to artificial sensory systems, enabling more natural and intuitive human-machine interactions and advancing the frontier of biomedical applications.

ACKNOWLEDGMENTS

This work was supported by the National Research Foundation of Korea (NRF) grant funded by the Korea government (MSIT) (No. RS-2024-00353768), KIST Institutional Program (Project No. 2E31603-22-140). This work was supported by the Yonsei Fellowship, funded by Lee Youn Jae.

AUTHOR DECLARATIONS

Conflict of Interest

The authors have no conflicts to disclose.

Author Contributions

Kyowon Kang and Kiho Kim contributed equally to this work.

Kyowon Kang: Conceptualization (equal); Formal analysis (equal); Investigation (equal); Project administration (equal); Validation (equal); Visualization (equal); Writing – original draft (equal); Writing – review & editing (equal). **Kiho Kim:** Conceptualization (equal); Data curation (equal); Formal analysis (equal); Investigation (equal); Project administration (equal); Validation (equal); Visualization (equal); Writing – original draft (equal); Writing – review & editing (equal). **Junhyeong Baek:** Investigation (supporting); Visualization (supporting). **Doohyun J. Lee:** Investigation (supporting); Visualization (supporting). **Ki Jun Yu:** Conceptualization (equal); Funding acquisition (lead); Project administration (lead); Supervision (lead); Writing – review & editing (equal).

DATA AVAILABILITY

The data that support the findings of this study are available from the corresponding author upon reasonable request.

REFERENCES

- ¹S. Herculano-Houzel, “The remarkable, yet not extraordinary, human brain as a scaled-up primate brain and its associated cost,” *Proc. Natl. Acad. Sci. U. S. A.* **109**, 10661–10668 (2012).
- ²S. Herculano-Houzel, “The human brain in numbers: A linearly scaled-up primate brain,” *Front. Hum. Neurosci.* **3**, 31 (2009).
- ³C. S. von Bartheld, J. Bahney, and S. Herculano-Houzel, “The search for true numbers of neurons and glial cells in the human brain: A review of 150 years of cell counting,” *J. Comp. Neurol.* **524**(18), 3865–3895 (2016).
- ⁴K. Siletti, R. Hodge, A. Mossi Albiach, K. W. Lee, S.-L. Ding, L. Hu, P. Lönnberg, T. Bakken, T. Casper, M. Clark, N. Dee, J. Gloe, D. Hirschstein, N. V. Shapovalova, C. D. Keene, J. Nyhus, H. Tung, A. M. Yanny, E. Arenas,

- E. S. Lein, and S. Linnarsson, "Transcriptomic diversity of cell types across the adult human brain," *Science* **382**(6667), eadd7046 (2023).
- ⁵Y. E. Li, S. Preissl, M. Miller, N. D. Johnson, Z. Wang, H. Jiao, C. Zhu, Z. Wang, Y. Xie, O. Poirion, C. Kern, A. Pinto-Duarte, W. Tian, K. Siletti, N. Emerson, J. Osteen, J. Lucero, L. Lin, Q. Yang, Q. Zhu, N. Zemke, S. Espinoza, A. M. Yanny, J. Nyhus, N. Dee, T. Casper, N. Shapovalova, D. Hirschstein, R. D. Hodge, S. Linnarsson, T. Bakken, B. Levi, C. D. Keene, J. Shang, E. Lein, A. Wang, M. M. Behrens, J. R. Ecker, and B. Ren, "A comparative atlas of single-cell chromatin accessibility in the human brain," *Science* **382**(6667), eadf7044 (2023).
- ⁶W. Tian, J. Zhou, A. Bartlett, Q. Zeng, H. Liu, R. G. Castanon, M. Kenworthy, J. Altshul, C. Valadon, A. Aldridge, J. R. Nery, H. Chen, J. Xu, N. D. Johnson, J. Lucero, J. K. Osteen, N. Emerson, J. Rink, J. Lee, Y. E. Li, K. Siletti, M. Liem, N. Claffey, C. O'Connor, A. M. Yanny, J. Nyhus, N. Dee, T. Casper, N. Shapovalova, D. Hirschstein, S.-L. Ding, R. Hodge, B. P. Levi, C. D. Keene, S. Linnarsson, E. Lein, B. Ren, M. M. Behrens, and J. R. Ecker, "Single-cell DNA methylation and 3D genome architecture in the human brain," *Science* **382**(6667), eadf5357 (2023).
- ⁷D. Ielmini and S. Ambrogio, "Emerging neuromorphic devices," *Nanotechnology* **31**(9), 092001 (2020).
- ⁸I.-J. Kim and J.-S. Lee, "Ferroelectric transistors for memory and neuromorphic device applications," *Adv. Mater.* **35**(22), 2206864 (2023).
- ⁹M.-K. Kim, Y. Park, I.-J. Kim, and J.-S. Lee, "Emerging materials for neuromorphic devices and systems," *iScience* **23**(12), 101846 (2020).
- ¹⁰V. K. Sangwan and M. C. Hersam, "Neuromorphic nanoelectronic materials," *Nat. Nanotechnol.* **15**(7), 517–528 (2020).
- ¹¹F. Sun, Q. Lu, S. Feng, and T. Zhang, "Flexible artificial sensory systems based on neuromorphic devices," *ACS Nano* **15**(3), 3875–3899 (2021).
- ¹²Y. van de Burgt, E. Lubberman, E. J. Fuller, S. T. Keene, G. C. Faria, S. Agarwal, M. J. Marinella, A. Alec Talin, and A. Salleo, "A non-volatile organic electrochemical device as a low-voltage artificial synapse for neuromorphic computing," *Nat. Mater.* **16**(4), 414–418 (2017).
- ¹³Y. van de Burgt, A. Melianas, S. T. Keene, G. Malliaras, and A. Salleo, "Organic electronics for neuromorphic computing," *Nat. Electron.* **1**(7), 386–397 (2018).
- ¹⁴J. Zhu, T. Zhang, Y. Yang, and R. Huang, "A comprehensive review on emerging artificial neuromorphic devices," *Appl. Phys. Rev.* **7**(1), 011312 (2020).
- ¹⁵S. H. Kim, G. W. Baek, J. Yoon, S. Seo, J. Park, D. Hahn, J. H. Chang, D. Seong, H. Seo, S. Oh, K. Kim, H. Jung, Y. Oh, H. W. Baac, B. Alimkhanuly, W. K. Bae, S. Lee, M. Lee, J. Kwak, J.-H. Park, and D. Son, "A bioinspired stretchable sensory-neuromorphic system," *Adv. Mater.* **33**(44), 2104690 (2021).
- ¹⁶Y. R. Lee, T. Q. Trung, B.-U. Hwang, and N.-E. Lee, "A flexible artificial intrinsic-synaptic tactile sensory organ," *Nat. Commun.* **11**(1), 2753 (2020).
- ¹⁷J.-K. Han, I.-W. Tcho, S.-B. Jeon, J.-M. Yu, W.-G. Kim, and Y.-K. Choi, "Self-powered artificial mechanoreceptor based on triboelectrification for a neuromorphic tactile system," *Adv. Sci.* **9**(9), 2105076 (2022).
- ¹⁸W. W. Lee, Y. J. Tan, H. Yao, S. Li, H. H. See, M. Hon, K. A. Ng, B. Xiong, J. S. Ho, and B. C. K. Tee, "A neuro-inspired artificial peripheral nervous system for scalable electronic skins," *Sci. Rob.* **4**(32), eaax2198 (2019).
- ¹⁹Y. Kim, A. Chortos, W. Xu, Y. Liu, J. Y. Oh, D. Son, J. Kang, A. M. Foudeh, C. Zhu, Y. Lee, S. Niu, J. Liu, R. Pfattner, Z. Bao, and T.-W. Lee, "A bioinspired flexible organic artificial afferent nerve," *Science* **360**(6392), 998–1003 (2018).
- ²⁰W. Wang, Y. Jiang, D. Zhong, Z. Zhang, S. Choudhury, J.-C. Lai, H. Gong, S. Niu, X. Yan, Y. Zheng, C.-C. Shih, R. Ning, Q. Lin, D. Li, Y.-H. Kim, J. Kim, Y.-X. Wang, C. Zhao, C. Xu, X. Ji, Y. Nishio, H. Lyu, J. B.-H. Tok, and Z. Bao, "Neuromorphic sensorimotor loop embodied by monolithically integrated, low-voltage, soft e-skin," *Science* **380**(6646), 735–742 (2023).
- ²¹K. Kang, S. Ye, C. Jeong, J. Jeong, Y.-s. Ye, J.-Y. Jeong, Y.-J. Kim, S. Lim, T. H. Kim, K. Y. Kim, J. U. Kim, G. I. Kim, D. H. Chun, K. Kim, J. Park, J.-H. Hong, B. Park, K. Kim, S. Jung, K. Baek, D. Cho, J. Yoo, K. Lee, H. Cheng, B.-W. Min, H. J. Kim, H. Jeon, H. Yi, T.-i. Kim, K. J. Yu, and Y. Jung, "Bionic artificial skin with a fully implantable wireless tactile sensory system for wound healing and restoring skin tactile function," *Nat. Commun.* **15**(1), 10 (2024).
- ²²S. Chun, J.-S. Kim, Y. Yoo, Y. Choi, S. J. Jung, D. Jang, G. Lee, K.-I. Song, K. S. Nam, and I. Youn, "An artificial neural tactile sensing system," *Nat. Electron.* **4**(6), 429–438 (2021).
- ²³N. Bai, L. Wang, Q. Wang, J. Deng, Y. Wang, P. Lu, J. Huang, G. Li, Y. Zhang, and J. Yang, "Graded intrafillable architecture-based iontronic pressure sensor with ultra-broad-range high sensitivity," *Nat. Commun.* **11**(1), 209 (2020).
- ²⁴R. Yang, A. Dutta, B. Li, N. Tiwari, W. Zhang, Z. Niu, Y. Gao, D. Erdely, X. Xin, T. Li, and H. Cheng, "Iontronic pressure sensor with high sensitivity over ultra-broad linear range enabled by laser-induced gradient micro-pyramids," *Nat. Commun.* **14**(1), 2907 (2023).
- ²⁵R. Chen, T. Luo, J. Wang, R. Wang, C. Zhang, Y. Xie, L. Qin, H. Yao, and W. Zhou, "Nonlinearity synergy: An elegant strategy for realizing high-sensitivity and wide-linear-range pressure sensing," *Nat. Commun.* **14**(1), 6641 (2023).
- ²⁶Z. Wen, Y. Yang, N. Sun, G. Li, Y. Liu, C. Chen, J. Shi, L. Xie, H. Jiang, and D. Bao, "A wrinkled PEDOT: PSS film based stretchable and transparent triboelectric nanogenerator for wearable energy harvesters and active motion sensors," *Adv. Funct. Mater.* **28**(37), 1803684 (2018).
- ²⁷T. Li, M. Qu, C. Carlos, L. Gu, F. Jin, T. Yuan, X. Wu, J. Xiao, T. Wang, and W. Dong, "High-performance poly (vinylidene difluoride)/dopamine core/shell piezoelectric nanofiber and its application for biomedical sensors," *Adv. Mater.* **33**(3), 2006093 (2021).
- ²⁸K. Kang, J. Park, K. Kim, and K. J. Yu, "Recent developments of emerging inorganic, metal and carbon-based nanomaterials for pressure sensors and their healthcare monitoring applications," *Nano Res.* **14**(9), 3096–3111 (2021).
- ²⁹S.-H. Woo, S. Ranade, A. D. Weyer, A. E. Dubin, Y. Baba, Z. Qiu, M. Petrus, T. Miyamoto, K. Reddy, and E. A. Lumpkin, "Piezo2 is required for Merkel-cell mechanotransduction," *Nature* **509**(7502), 622–626 (2014).
- ³⁰V. B. Mountcastle, *The Sensory Hand: Neural Mechanisms of Somatic Sensation* (Harvard University Press, 2005).
- ³¹A. C. Guyton and J. E. Hall, *Pocket Companion to Textbook of Medical Physiology* (Saunders, 1998).
- ³²J. A. Vega, A. Lopez-Muniz, M. G. Calavia, O. Garcia-Suarez, J. Cobo, J. Otero, O. Arias-Carrion, P. Perez-Pinera, and M. Menendez-Gonzalez, "Clinical implication of Meissner's corpuscles," *CNS Neurol. Disord.* **11**(7), 856–868 (2012).
- ³³M. Paré, R. Elde, J. E. Mazurkiewicz, A. M. Smith, and F. L. Rice, "The Meissner corpuscle revised: A multiiafferent mechanoreceptor with nociceptor immunochemical properties," *J. Neurosci.* **21**(18), 7236–7246 (2001).
- ³⁴A. Zimmerman, L. Bai, and D. D. Ginty, "The gentle touch receptors of mammalian skin," *Science* **346**(6212), 950–954 (2014).
- ³⁵J. Scheibert, S. Leurent, A. Prevost, and G. Debrégeas, "The role of fingerprints in the coding of tactile information probed with a biomimetic sensor," *Science* **323**(5920), 1503–1506 (2009).
- ³⁶M. L. Jin, S. Park, Y. Lee, J. H. Lee, J. Chung, J. S. Kim, J. S. Kim, S. Y. Kim, E. Jee, and D. W. Kim, "An ultrasensitive, visco-poroelastic artificial mechanotransducer skin inspired by piezo2 protein in mammalian merkel cells," *Adv. Mater.* **29**(13), 1605973 (2017).
- ³⁷J. Park, M. Kim, Y. Lee, H. S. Lee, and H. Ko, "Fingertip skin-inspired microstructured ferroelectric skins discriminate static/dynamic pressure and temperature stimuli," *Sci. Adv.* **1**(9), e1500661 (2015).
- ³⁸Y. Li, M. Zhao, Y. Yan, L. He, Y. Wang, Z. Xiong, S. Wang, Y. Bai, F. Sun, Q. Lu, Y. Wang, T. Li, and T. Zhang, "Multifunctional biomimetic tactile system via a stick-slip sensing strategy for human-machine interactions," *npj Flexible Electron.* **6**(1), 46 (2022).
- ³⁹K. Kim, M. Sim, S.-H. Lim, D. Kim, D. Lee, K. Shin, C. Moon, J.-W. Choi, and J. E. Jang, "Tactile avatar: Tactile sensing system mimicking human tactile cognition," *Adv. Sci.* **8**(7), 2002362 (2021).
- ⁴⁰S. Kim, Y. Lee, H.-D. Kim, and S.-J. Choi, "A tactile sensor system with sensory neurons and a perceptual synaptic network based on semivolatile carbon nanotube transistors," *NPG Asia Mater.* **12**(1), 76 (2020).
- ⁴¹S. Oh, Y. Jung, S. Kim, X. Hu, H. Lim, and C. Kim, "Remote tactile sensing system integrated with magnetic synapse," *Sci. Rep.* **7**(1), 16963 (2017).
- ⁴²M. Kumar, R. Singh, H. Kang, S. Kim, and H. Seo, "An artificial piezotronic synapse for tactile perception," *Nano Energy* **73**, 104756 (2020).
- ⁴³H. Kim, S. Oh, H. Choo, D.-H. Kang, and J.-H. Park, "Tactile neuromorphic system: Convergence of triboelectric polymer sensor and ferroelectric polymer synapse," *ACS Nano* **17**(17), 17332–17341 (2023).
- ⁴⁴C. Wang, L. Dong, D. Peng, and C. Pan, "Tactile sensors for advanced intelligent systems," *Adv. Intell. Syst.* **1**(8), 1900090 (2019).

- ⁴⁵Z. Zhou, H. Zhang, J. Liu, and W. Huang, "Flexible electronics from intrinsically soft materials," *Giant* **6**, 100051 (2021).
- ⁴⁶Y. Zhao and X. Huang, "Mechanisms and materials of flexible and stretchable skin sensors," *Micromachines* **8**(3), 69 (2017).
- ⁴⁷K. Kang, M. Sang, B. Xu, and K. J. Yu, "Fabrication of gold-doped crystalline-silicon nanomembrane-based wearable temperature sensor," *STAR Protoc.* **4**(1), 101925 (2023).
- ⁴⁸M. Sang, K. Kang, Y. Zhang, H. Zhang, K. Kim, M. Cho, J. Shin, J.-H. Hong, T. Kim, S. K. Lee, W.-H. Yeo, J. W. Lee, T. Lee, B. Xu, and K. J. Yu, "Ultrahigh sensitive Au-doped silicon nanomembrane based wearable sensor arrays for continuous skin temperature monitoring with high precision," *Adv. Mater.* **34**(4), 2105865 (2022).
- ⁴⁹Y.-F. Fu, F.-L. Yi, J.-R. Liu, Y.-Q. Li, Z.-Y. Wang, G. Yang, P. Huang, N. Hu, and S.-Y. Fu, "Super soft but strong E-skin based on carbon fiber/carbon black/silicone composite: Truly mimicking tactile sensing and mechanical behavior of human skin," *Compos. Sci. Technol.* **186**, 107910 (2020).
- ⁵⁰F. Zhang, C. Li, Z. Li, L. Dong, and J. Zhao, "Recent progress in three-terminal artificial synapses based on 2D materials: From mechanisms to applications," *Microsyst. Nanoeng.* **9**(1), 16 (2023).
- ⁵¹S. Oh, J.-J. Lee, S. Seo, G. Yoo, and J.-H. Park, "Photoelectroactive artificial synapse and its application to biosignal pattern recognition," *npj 2D Mater. Appl.* **5**(1), 95 (2021).
- ⁵²S. Kim, K. Heo, S. Lee, S. Seo, H. Kim, J. Cho, H. Lee, K.-B. Lee, and J.-H. Park, "Ferroelectric polymer-based artificial synapse for neuromorphic computing," *Nanoscale Horiz.* **6**(2), 139–147 (2021).
- ⁵³Z. Guo, J. Liu, X. Han, F. Ma, D. Rong, J. Du, Y. Yang, T. Wang, G. Li, Y. Huang, and J. Xing, "High-performance artificial synapse based on CVD-grown WSe₂ flakes with intrinsic defects," *ACS Appl. Mater. Interfaces* **15**(15), 19152–19162 (2023).
- ⁵⁴J. Yu, X. Yang, G. Gao, Y. Xiong, Y. Wang, J. Han, Y. Chen, H. Zhang, Q. Sun, and Z. L. Wang, "Bioinspired mechano-photonic artificial synapse based on graphene/MoS₂ heterostructure," *Sci. Adv.* **7**(12), eabd9117 (2021).
- ⁵⁵S.-R. Zhang, L. Zhou, J.-Y. Mao, Y. Ren, J.-Q. Yang, G.-H. Yang, X. Zhu, S.-T. Han, V. A. L. Roy, and Y. Zhou, "Artificial synapse emulated by charge trapping-based resistive switching device," *Adv. Mater. Technol.* **4**(2), 1800342 (2019).
- ⁵⁶T. Birkbogen, H. Winterfeld, S. Fichtner, A. Petraru, and H. Kohlstedt, "A spiking and adapting tactile sensor for neuromorphic applications," *Sci. Rep.* **10**(1), 17260 (2020).
- ⁵⁷X. Wang, Z. Liu, and T. Zhang, "Flexible sensing electronics for wearable/attachable health monitoring," *Small* **13**(25), 1602790 (2017).
- ⁵⁸A. Chhetry, J. Kim, H. Yoon, and J. Y. Park, "Ultrasensitive interfacial capacitive pressure sensor based on a randomly distributed microstructured ion-tronic film for wearable applications," *ACS Appl. Mater. Interfaces* **11**(3), 3438–3449 (2018).
- ⁵⁹S. C. Mannsfeld, B. C. Tee, R. M. Stoltberg, C. V. H. Chen, S. Barman, B. V. Muir, A. N. Sokolov, C. Reese, and Z. Bao, "Highly sensitive flexible pressure sensors with microstructured rubber dielectric layers," *Nat. Mater.* **9**(10), 859–864 (2010).
- ⁶⁰W. Asghar, F. Li, Y. Zhou, Y. Wu, Z. Yu, S. Li, D. Tang, X. Han, J. Shang, and Y. Liu, "Piezocapacitive flexible e-skin pressure sensors having magnetically grown microstructures," *Adv. Mater. Technol.* **5**(2), 1900934 (2020).
- ⁶¹Y. Ma, Z. Li, S. Tu, T. Zhu, W. Xu, M. Chen, L. Shi, and L. Wu, "An asymmetric interlocked structure with modulus gradient for ultrawide piezocapacitive pressure sensing applications," *Adv. Funct. Mater.* **34**, 2309792 (2023).
- ⁶²G. Arias-Ferreiro, A. Ares-Pernas, A. Lasagabáster-Latorre, M. S. Dopico-García, P. Ligero, N. Pereira, P. Costa, S. Lanceros-Mendez, and M. J. Abad, "Photocurable printed piezocapacitive pressure sensor based on an acrylic resin modified with polyaniline and lignin," *Adv. Mater. Technol.* **7**(8), 2101503 (2022).
- ⁶³J. He, Y. Zhang, R. Zhou, L. Meng, T. Chen, W. Mai, and C. Pan, "Recent advances of wearable and flexible piezoresistivity pressure sensor devices and its future prospects," *J. Materiomics* **6**(1), 86–101 (2020).
- ⁶⁴L. Yuan, Z. Wang, H. Li, Y. Huang, S. Wang, X. Gong, Z. Tan, Y. Hu, X. Chen, and J. Li, "Synergistic resistance modulation toward ultrahighly sensitive piezoresistive pressure sensors," *Adv. Mater. Technol.* **5**(4), 1901084 (2020).
- ⁶⁵W.-G. Kim, D.-W. Kim, I.-W. Tcho, J.-K. Kim, M.-S. Kim, and Y.-K. Choi, "Triboelectric nanogenerator: Structure, mechanism, and applications," *ACS Nano* **15**(1), 258–287 (2021).
- ⁶⁶Z. Zhao, L. Zhou, S. Li, D. Liu, Y. Li, Y. Gao, Y. Liu, Y. Dai, J. Wang, and Z. L. Wang, "Selection rules of triboelectric materials for direct-current triboelectric nanogenerator," *Nat. Commun.* **12**(1), 4686 (2021).
- ⁶⁷J. Li, Z. Yuan, X. Han, C. Wang, Z. Huo, Q. Lu, M. Xiong, X. Ma, W. Gao, and C. Pan, "Biologically inspired stretchable, multifunctional, and 3D electronic skin by strain visualization and triboelectric pressure sensing," *Small Sci.* **2**(1), 2100083 (2022).
- ⁶⁸J. Jiang, S. Tu, R. Fu, J. Li, F. Hu, B. Yan, Y. Gu, and S. Chen, "Flexible piezoelectric pressure tactile sensor based on electrospun BaTiO₃/poly(vinylidene fluoride) nanocomposite membrane," *ACS Appl. Mater. Interfaces* **12**(30), 33989–33998 (2020).
- ⁶⁹Y. Mao, P. Zhao, G. McConohy, H. Yang, Y. Tong, and X. Wang, "Sponge-like piezoelectric polymer films for scalable and integratable nanogenerators and self-powered electronic systems," *Adv. Energy Mater.* **4**(7), 1301624 (2014).
- ⁷⁰K. Meng, X. Xiao, W. Wei, G. Chen, A. Nashalian, S. Shen, X. Xiao, and J. Chen, "Wearable pressure sensors for pulse wave monitoring," *Adv. Mater.* **34**(21), 2109357 (2022).
- ⁷¹K. H. Ha, W. Zhang, H. Jang, S. Kang, L. Wang, P. Tan, H. Hwang, and N. Lu, "Highly sensitive capacitive pressure sensors over a wide pressure range enabled by the hybrid responses of a highly porous nanocomposite," *Adv. Mater.* **33**(48), 2103320 (2021).
- ⁷²G. Y. Bae, S. W. Pak, D. Kim, G. Lee, D. H. Kim, Y. Chung, and K. Cho, "Linearly and highly pressure-sensitive electronic skin based on a bioinspired hierarchical structural array," *Adv. Mater.* **28**(26), 5300–5306 (2016).
- ⁷³L. Dan, S. Shi, H.-J. Chung, and A. Elias, "Porous polydimethylsiloxane–silver nanowire devices for wearable pressure sensors," *ACS Appl. Nano Mater.* **2**(8), 4869–4878 (2019).
- ⁷⁴Z. Qiu, Y. Wan, W. Zhou, J. Yang, J. Yang, J. Huang, J. Zhang, Q. Liu, S. Huang, and N. Bai, "Ionic skin with biomimetic dielectric layer templated from calathea zebrina leaf," *Adv. Funct. Mater.* **28**(37), 1802343 (2018).
- ⁷⁵B. Zou, Y. Chen, Y. Liu, R. Xie, Q. Du, T. Zhang, Y. Shen, B. Zheng, S. Li, and J. Wu, "Repurposed leather with sensing capabilities for multifunctional electronic skin," *Adv. Sci.* **6**(3), 1801283 (2019).
- ⁷⁶W. Liu, N. Liu, Y. Yue, J. Rao, F. Cheng, J. Su, Z. Liu, and Y. Gao, "Piezoresistive pressure sensor based on synergistical innerconnect polyvinyl alcohol nanowires/wrinkled graphene film," *Small* **14**(15), 1704149 (2018).
- ⁷⁷B. Ji, Q. Zhou, B. Hu, J. Zhong, J. Zhou, and B. Zhou, "Bio-inspired hybrid dielectric for capacitive and triboelectric tactile sensors with high sensitivity and ultrawide linearity range," *Adv. Mater.* **33**(27), 2100859 (2021).
- ⁷⁸Y. Zhang, J. Yang, X. Hou, G. Li, L. Wang, N. Bai, M. Cai, L. Zhao, Y. Wang, and J. Zhang, "Highly stable flexible pressure sensors with a quasi-homogeneous composition and interlinked interfaces," *Nat. Commun.* **13**(1), 1317 (2022).
- ⁷⁹J. Xu, H. Li, Y. Yin, X. Li, J. Cao, H. Feng, W. Bao, H. Tan, F. Xiao, and G. Zhu, "High sensitivity and broad linearity range pressure sensor based on hierarchical in-situ filling porous structure," *npj Flexible Electron.* **6**(1), 62 (2022).
- ⁸⁰M. Fu, J. Zhang, Y. Jin, Y. Zhao, S. Huang, and C. F. Guo, "A highly sensitive, reliable, and high-temperature-resistant flexible pressure sensor based on ceramic nanofibers," *Adv. Sci.* **7**(17), 2000258 (2020).
- ⁸¹S. S. Ranade, R. Syeda, and A. Patapoutian, "Mechanically activated ion channels," *Neuron* **87**(6), 1162–1179 (2015).
- ⁸²K. Schrenk-Siemens, H. Wende, V. Prato, K. Song, C. Rostock, A. Loewer, J. Utikal, G. R. Lewin, S. G. Lechner, and J. Siemens, "PIEZ02 is required for mechanotransduction in human stem cell-derived touch receptors," *Nat. Neurosci.* **18**(1), 10–16 (2015).
- ⁸³R. Ikeda, M. Cha, J. Ling, Z. Jia, D. Coyle, and J. G. Gu, "Merkel cells transduce and encode tactile stimuli to drive A β -afferent impulses," *Cell* **157**(3), 664–675 (2014).
- ⁸⁴S. Katta, M. Krieg, and M. B. Goodman, "Feeling force: Physical and physiological principles enabling sensory mechanotransduction," *Annu. Rev. Cell Dev. Biol.* **31**, 347–371 (2015).

- ⁸⁵S.-H. Woo, E. A. Lumpkin, and A. Patapoutian, "Merkel cells and neurons keep in touch," *Trends Cell Biol.* **25**(2), 74–81 (2015).
- ⁸⁶Y. A. Nikolaev, V. V. Feketa, E. O. Anderson, E. R. Schneider, E. O. Gracheva, and S. N. Bagriantsev, "Lamellar cells in Pacinian and Meissner corpuscles are touch sensors," *Sci. Adv.* **6**(51), eabe6393 (2020).
- ⁸⁷V. E. Abraira and D. D. Ginty, "The sensory neurons of touch," *Neuron* **79**(4), 618–639 (2013).
- ⁸⁸S. Chun, W. Son, H. Kim, S. K. Lim, C. Pang, and C. Choi, "Self-powered pressure-and vibration-sensitive tactile sensors for learning technique-based neural finger skin," *Nano Lett.* **19**(5), 3305–3312 (2019).
- ⁸⁹L. Gallo and M. Sebastian, "A., An overview of phase-change memory device physics," *J. Phys. D* **53**(21), 213002 (2020).
- ⁹⁰N. Ciocchini, M. Laudato, M. Bonardi, E. Varesi, P. Fantini, A. L. Lacaita, and D. Ielmini, "Bipolar switching in chalcogenide phase change memory," *Sci. Rep.* **6**(1), 29162 (2016).
- ⁹¹A. I. Khan, A. Daus, R. Islam, K. M. Neilson, H. R. Lee, H.-S. P. Wong, and E. Pop, "Ultralow-switching current density multilevel phase-change memory on a flexible substrate," *Science* **373**(6560), 1243–1247 (2021).
- ⁹²K. Moon, S. Lim, J. Park, C. Sung, S. Oh, J. Woo, J. Lee, and H. Hwang, "RRAM-based synapse devices for neuromorphic systems," *Faraday Discuss.* **213**(0), 421–451 (2019).
- ⁹³D. Ielmini, "Brain-inspired computing with resistive switching memory (RRAM): Devices, synapses and neural networks," *Microelectron. Eng.* **190**, 44–53 (2018).
- ⁹⁴J. F. Kang, B. Gao, P. Huang, L. F. Liu, X. Y. Liu, H. Y. Yu, S. Yu, and H. S. P. Wong, in "RRAM based synaptic devices for neuromorphic visual systems," in *2015 IEEE International Conference on Digital Signal Processing (DSP)* (IEEE, 2015), pp 1219–1222.
- ⁹⁵S. Lequeux, J. Sampao, V. Cros, K. Yakushiji, A. Fukushima, R. Matsumoto, H. Kubota, S. Yuasa, and J. Grollier, "A magnetic synapse: Multilevel spin-torque memristor with perpendicular anisotropy," *Sci. Rep.* **6**(1), 31510 (2016).
- ⁹⁶A. Vincent, J. F. Larroque, N. Locatelli, N. Ben Romdhane, O. Bichler, C. Gamrat, W. Zhao, J.-O. Klein, S. Galdin-Retailleau, and D. Querlioz, "Spin-transfer torque magnetic memory as a stochastic memristive synapse for neuromorphic systems," *IEEE Trans. Biomed. Circuits Syst.* **9**(2), 166–174 (2015).
- ⁹⁷P. Krzysteczk, J. Münchenberger, M. Schäfers, G. Reiss, and A. Thomas, "The memristive magnetic tunnel junction as a nanoscopic synapse-neuron system," *Adv. Mater.* **24**(6), 762–766 (2012).
- ⁹⁸S. G. Sarwat, B. Kersting, T. Moraitis, V. P. Jonnalagadda, and A. Sebastian, "Phase-change memristive synapses for mixed-plasticity neural computations," *Nat. Nanotechnol.* **17**(5), 507–513 (2022).
- ⁹⁹D. Kuzum, R. G. D. Jeyasingh, B. Lee, and H. S. P. Wong, "Nanoelectronic programmable synapses based on phase change materials for brain-inspired computing," *Nano Lett.* **12**(5), 2179–2186 (2012).
- ¹⁰⁰M. Suri, O. Bichler, D. Querlioz, O. Cueto, L. Perniola, V. Sousa, D. Vuillaume, C. Gamrat, and B. DeSalvo, "Phase change memory as synapse for ultra-dense neuromorphic systems: Application to complex visual pattern extraction," in *International Electron Devices Meeting* (IEEE, 2011), pp. 4.4.1–4.4.4.
- ¹⁰¹S. X. Go, T. H. Lee, S. R. Elliott, N. Bajalovic, and D. K. Loke, "A fast, low-energy multi-state phase-change artificial synapse based on uniform partial-state transitions," *APL Mater.* **9**(9), 091103 (2021).
- ¹⁰²H. Han, H. Yu, H. Wei, J. Gong, and W. Xu, "Recent progress in three-terminal artificial synapses: From device to system," *Small* **15**(32), 1900695 (2019).
- ¹⁰³L. Liu, P. A. Dananjaya, C. C. I. Ang, E. K. Koh, G. J. Lim, H. Y. Poh, M. Y. Chee, C. X. X. Lee, and W. S. Lew, "A bi-functional three-terminal memristor applicable as an artificial synapse and neuron," *Nanoscale* **15**(42), 17076–17084 (2023).
- ¹⁰⁴J. Li, Z. Shen, Y. Cao, X. Tu, C. Zhao, Y. Liu, and Z. Wen, "Artificial synapses enabled neuromorphic computing: From blueprints to reality," *Nano Energy* **103**, 107744 (2022).
- ¹⁰⁵C. Wu, T. W. Kim, H. Y. Choi, D. B. Strukov, and J. J. Yang, "Flexible three-dimensional artificial synapse networks with correlated learning and trainable memory capability," *Nat. Commun.* **8**(1), 752 (2017).
- ¹⁰⁶D. Carta, I. Salaoru, A. Khiat, A. Regoutz, C. Mitterbauer, N. M. Harrison, and T. Prodromakis, "Investigation of the switching mechanism in TiO₂-based RRAM: A two-dimensional EDX approach," *ACS Appl. Mater. Interfaces* **8**(30), 19605–19611 (2016).
- ¹⁰⁷D. Acharyya, A. Hazra, and P. Bhattacharyya, "A journey towards reliability improvement of TiO₂ based resistive random access memory: A review," *Microelectron. Reliab.* **54**(3), 541–560 (2014).
- ¹⁰⁸B. Jiang, J. Iocozzia, L. Zhao, H. Zhang, Y.-W. Harn, Y. Chen, and Z. Lin, "Barium titanate at the nanoscale: Controlled synthesis and dielectric and ferroelectric properties," *Chem. Soc. Rev.* **48**(4), 1194–1228 (2019).
- ¹⁰⁹Y. Tan, J. Zhang, Y. Wu, C. Wang, V. Koval, B. Shi, H. Ye, R. McKinnon, G. Viola, and H. Yan, "Unfolding grain size effects in barium titanate ferroelectric ceramics," *Sci. Rep.* **5**(1), 9953 (2015).
- ¹¹⁰G. H. Kwei, A. C. Lawson, S. J. L. Billinge, and S. W. Cheong, "Structures of the ferroelectric phases of barium titanate," *J. Phys. Chem.* **97**(10), 2368–2377 (1993).
- ¹¹¹J. Yang, S. Liu, Y. Meng, W. Xu, S. Liu, L. Jia, G. Chen, Y. Qin, M. Han, and X. Li, "Self-powered tactile sensor for gesture recognition using deep learning algorithms," *ACS Appl. Mater. Interfaces* **14**(22), 25629–25637 (2022).
- ¹¹²A. Schmitz, Y. Bansho, K. Noda, H. Iwata, T. Ogata, and S. Sugano, "Tactile object recognition using deep learning and dropout," in *IEEE-RAS International Conference on Humanoid Robots* (IEEE, 2014), pp. 1044–1050.
- ¹¹³T. Zhang, M. Zhao, M. Zhai, L. Wang, X. Ma, S. Liao, X. Wang, Y. Liu, and D. Chen, "Improving the resolution of flexible large-area tactile sensors through machine-learning perception," *ACS Appl. Mater. Interfaces* **16**, 11013–11025 (2024).
- ¹¹⁴Z. Hu, L. Lin, W. Lin, Y. Xu, X. Xia, Z. Peng, Z. Sun, and Z. Wang, "Machine learning for tactile perception: Advancements, challenges, and opportunities," *Adv. Intell. Syst.* **5**(7), 2200371 (2023).
- ¹¹⁵Z. Ding and Z. Zhang, "2D tactile sensor based on multimode interference and deep learning," *Opt. Laser Technol.* **136**, 106760 (2021).
- ¹¹⁶H. Sun, K. J. Kuchenbecker, and G. Martius, "A soft thumb-sized vision-based sensor with accurate all-round force perception," *Nat. Mach. Intell.* **4**(2), 135–145 (2022).
- ¹¹⁷W. W. Lee, S. L. Kukreja, and N. V. Thakor, "Discrimination of dynamic tactile contact by temporally precise event sensing in spiking neuromorphic networks," *Front. Neurosci.* **11**, 5 (2017).
- ¹¹⁸D. W. Kim, J. C. Yang, S. Lee, and S. Park, "Neuromorphic processing of pressure signal using integrated sensor-synaptic device capable of selective and reversible short- and long-term plasticity operation," *ACS Appl. Mater. Interfaces* **12**(20), 23207–23216 (2020).
- ¹¹⁹M. Zeng, Y. He, C. Zhang, and Q. Wan, "Neuromorphic devices for bionic sensing and perception," *Front. Neurosci.* **15**, 690950 (2021).
- ¹²⁰S. Yang, J. Shin, T. Kim, K.-W. Moon, J. Kim, G. Jang, D. S. Hyeon, J. Yang, C. Hwang, Y. Jeong, and J. P. Hong, "Integrated neuromorphic computing networks by artificial spin synapses and spin neurons," *NPG Asia Mater.* **13**(1), 11 (2021).
- ¹²¹S. Ham, M. Kang, S. Jang, J. Jang, S. Choi, T.-W. Kim, and G. Wang, "One-dimensional organic artificial multi-synapses enabling electronic textile neural network for wearable neuromorphic applications," *Sci. Adv.* **6**(28), eaba1178 (2020).
- ¹²²T. Jin, Z. Sun, L. Li, Q. Zhang, M. Zhu, Z. Zhang, G. Yuan, T. Chen, Y. Tian, X. Hou, and C. Lee, "Triboelectric nanogenerator sensors for soft robotics aiming at digital twin applications," *Nat. Commun.* **11**(1), 5381 (2020).
- ¹²³Z. Song, J. Yin, Z. Wang, C. Lu, Z. Yang, Z. Zhao, Z. Lin, J. Wang, C. Wu, J. Cheng, Y. Dai, Y. Zi, S.-L. Huang, X. Chen, J. Song, G. Li, and W. Ding, "A flexible triboelectric tactile sensor for simultaneous material and texture recognition," *Nano Energy* **93**, 106798 (2022).
- ¹²⁴T. Li, J. Zou, F. Xing, M. Zhang, X. Cao, N. Wang, and Z. L. Wang, "From dual-mode triboelectric nanogenerator to smart tactile sensor: A multiplexing design," *ACS Nano* **11**(4), 3950–3956 (2017).
- ¹²⁵D. W. Kim, J. H. Lee, J. K. Kim, and U. Jeong, "Material aspects of triboelectric energy generation and sensors," *NPG Asia Mater.* **12**(1), 6 (2020).
- ¹²⁶S. Lee and J.-W. Park, "Fingerprint-inspired triboelectric nanogenerator with a geometrically asymmetric electrode design for a self-powered dynamic pressure sensor," *Nano Energy* **101**, 107546 (2022).

- ¹²⁷L. Dhakar, S. Gudla, X. Shan, Z. Wang, F. E. H. Tay, C.-H. Heng, and C. Lee, "Large scale triboelectric nanogenerator and self-powered pressure sensor array using low cost roll-to-roll UV embossing," *Sci. Rep.* **6**(1), 22253 (2016).
- ¹²⁸K. S. Shim, I. Y. Chung, and Y. J. Park, "A BJT-based heterostructure 1T-DRAM for low-voltage operation," *IEEE Electron Device Lett.* **33**(1), 14–16 (2012).
- ¹²⁹G. Giusi, "Physical insights of body effect and charge degradation in floating-body DRAMs," *Solid-State Electron.* **95**, 1–7 (2014).
- ¹³⁰Q. Duan, Z. Jing, X. Zou, Y. Wang, K. Yang, T. Zhang, S. Wu, R. Huang, and Y. Yang, "Spiking neurons with spatiotemporal dynamics and gain modulation for monolithically integrated memristive neural networks," *Nat. Commun.* **11**(1), 3399 (2020).
- ¹³¹R. De Col, K. Messlinger, and R. W. Carr, "Repetitive activity slows axonal conduction velocity and concomitantly increases mechanical activation threshold in single axons of the rat cranial dura," *J. Physiol.* **590**(4), 725–736 (2012).
- ¹³²K. Chida, K. Kaneko, S. Fujii, and Y. Yamazaki, "Activity-dependent modulation of the axonal conduction of action potentials along rat hippocampal mossy fibers," *Eur. J. Neurosci.* **41**(1), 45–54 (2015).
- ¹³³D. J. Bakkum, Z. C. Chao, and S. M. Potter, "Long-term activity-dependent plasticity of action potential propagation delay and amplitude in cortical networks," *PLoS One* **3**(5), e2088 (2008).
- ¹³⁴R. Benosman, S.-H. Ieng, C. Clercq, C. Bartolozzi, and M. Srinivasan, "Asynchronous frameless event-based optical flow," *Neural Networks* **27**, 32–37 (2012).
- ¹³⁵K. K. W. Ng, X. Tee, R. M. Vickery, and I. Birznieks, "The relationship between tactile intensity perception and afferent spike count is moderated by a function of frequency," *IEEE Trans. Haptics* **15**(1), 14–19 (2022).
- ¹³⁶S. J. Bensmaia, "Tactile intensity and population codes," *Behav. Brain Res.* **190**(2), 165–173 (2008).
- ¹³⁷S. Ray, S. S. Hsiao, N. E. Crone, P. J. Franaszczuk, and E. Niebur, "Effect of stimulus intensity on the spike-local field potential relationship in the secondary somatosensory cortex," *J. Neurosci.* **28**(29), 7334–7343 (2008).
- ¹³⁸S. Bensmaia, M. Hollins, and J. Yau, "Vibrotactile intensity and frequency information in the Pacinian system: A psychophysical model," *Percept. Psychophys.* **67**(5), 828–841 (2005).
- ¹³⁹T. Manos, M. Zeitler, and P. A. Tass, "How stimulation frequency and intensity impact on the long-lasting effects of coordinated reset stimulation," *PLoS Comput. Biol.* **14**(5), e1006113 (2018).
- ¹⁴⁰H. Tan, Q. Tao, I. Pande, S. Majumdar, F. Liu, Y. Zhou, P. O. Å. Persson, J. Rosen, and S. van Dijken, "Tactile sensory coding and learning with bio-inspired optoelectronic spiking afferent nerves," *Nat. Commun.* **11**(1), 1369 (2020).
- ¹⁴¹Y. Wu, Y. Liu, Y. Zhou, Q. Man, C. Hu, W. Asghar, F. Li, Z. Yu, J. Shang, G. Liu, M. Liao, and R.-W. Li, "A skin-inspired tactile sensor for smart prosthetics," *Sci. Rob.* **3**(22), eaat0429 (2018).
- ¹⁴²I. Shlomy, S. Divald, K. Tadmor, Y. Leichtmann-Bardoogo, A. Arami, and B. M. Maoz, "Restoring tactile sensation using a triboelectric nanogenerator," *ACS Nano* **15**(7), 11087–11098 (2021).
- ¹⁴³T.-D. Nguyen and J. S. Lee, "Recent development of flexible tactile sensors and their applications," *Sensors* **22**(1), 50 (2022).
- ¹⁴⁴S. Kamran and N. Ghaderi, "A novel high speed CMOS pseudo-differential ring VCO with wide tuning control voltage range," in *Iranian Conference on Electrical Engineering (ICEE)* (IEEE, 2017), pp. 201–204.
- ¹⁴⁵J. Borgmans, R. Riem, and P. Rombouts, "The analog behavior of pseudo digital ring oscillators used in VCO ADCs," *IEEE Trans. Circuits Syst. I* **68**(7), 2827–2840 (2021).
- ¹⁴⁶T. C. Huang, K. Fukuda, C. M. Lo, Y. H. Yeh, T. Sekitani, T. Someya, and K. T. Cheng, "Pseudo-CMOS: A novel design style for flexible electronics," in *Design, Automation & Test in Europe Conference & Exhibition (DATE 2010)* (IEEE, 2010), pp. 154–159.
- ¹⁴⁷K. Fukuda, T. Sekitani, T. Yokota, K. Kuribara, T. C. Huang, T. Sakurai, U. Zschieschang, H. Klauk, M. Ikeda, H. Kuwabara, T. Yamamoto, K. Takimiya, K. T. Cheng, and T. Someya, "Organic pseudo-CMOS circuits for low-voltage large-gain high-speed operation," *IEEE Electron Device Lett.* **32**(10), 1448–1450 (2011).
- ¹⁴⁸Y. Wang, X. Ma, Y. Jiang, W. Zang, P. Cao, M. Tian, N. Ning, and L. Zhang, "Dielectric elastomer actuators for artificial muscles: A comprehensive review of soft robot explorations," *Resour. Chem. Mater.* **1**(3), 308–324 (2022).
- ¹⁴⁹D. Yang, X. Kong, Y. Ni, D. Gao, B. Yang, Y. Zhu, and L. Zhang, "Novel nitrile-butadiene rubber composites with enhanced thermal conductivity and high dielectric constant," *Composites, Part A* **124**, 105447 (2019).
- ¹⁵⁰M. Zhang, J. Sun, G. Zhao, Y. Tong, X. Wang, H. Yu, P. Xue, X. Zhao, Q. Tang, and Y. Liu, "Dielectric design of high dielectric constant poly(urea-urethane) elastomer for low-voltage high-mobility intrinsically stretchable all-solution-processed organic transistors," *Small* (published online).
- ¹⁵¹J. Won, S. W. Choi, Y. S. Kang, H. Y. Ha, I.-H. Oh, H. S. Kim, K. T. Kim, and W. H. Jo, "Structural characterization and surface modification of sulfonated polystyrene-(ethylene-butylene)-styrene triblock proton exchange membranes," *J. Membr. Sci.* **214**(2), 245–257 (2003).
- ¹⁵²M. Inutsuka, K. Inoue, Y. Hayashi, A. Inomata, Y. Sakai, H. Yokoyama, and K. Ito, "Highly dielectric and flexible polyrotaxane elastomer by introduction of cyano groups," *Polymer* **59**, 10–15 (2015).
- ¹⁵³J. Xu, S. Wang, G.-J. N. Wang, C. Zhu, S. Luo, L. Jin, X. Gu, S. Chen, V. R. Feig, J. W. F. To, S. Rondeau-Gagné, J. Park, B. C. Schroeder, C. Lu, J. Y. Oh, Y. Wang, Y.-H. Kim, H. Yan, R. Sinclair, D. Zhou, G. Xue, B. Murmann, C. Linder, W. Cai, J. B.-H. Tok, J. W. Chung, and Z. Bao, "Highly stretchable polymer semiconductor films through the nanoconfinement effect," *Science* **355**(6320), 59–64 (2017).
- ¹⁵⁴J. Jeong, T. H. Kim, S. Park, J. Lee, U. Chae, J.-Y. Jeong, S. Park, S. Kim, I.-J. Cho, Y. Jung, and H. Yi, "Hybrid neural interfacing devices based on Au wires with nanograngular Au shell and hydrogel layer for anti-inflammatory and bi-directional neural communications," *Chem. Eng. J.* **465**, 142966 (2023).
- ¹⁵⁵J. X. Law, F. Musa, B. H. I. Ruszymah, A. J. El Haj, and Y. Yang, "A comparative study of skin cell activities in collagen and fibrin constructs," *Med. Eng. Phys.* **38**(9), 854–861 (2016).
- ¹⁵⁶H. Débels, M. Hamdi, K. Abberton, and W. Morrison, "Dermal matrices and bioengineered skin substitutes: A critical review of current options," *Plast. Reconstr. Surg.* **3**(1), e284 (2015).
- ¹⁵⁷A. Przekora, "A concise review on tissue engineered artificial skin grafts for chronic wound treatment: Can we reconstruct functional skin tissue in vitro?," *Cells* **9**(7), 1622 (2020).